2009

# Photonic crystal back-reflectors for light management and enhanced absorption in a-Si:H solar cells

Benjamin Michael Curtin
*Iowa State University*

**Photonic crystal back-reflectors for light management and enhanced absorption in a-Si:H solar cells**

by

Benjamin Michael Curtin

A thesis submitted to the graduate faculty

in partial fulfillment of the requirements for the degree of

MASTER OF SCIENCE

Major: Electrical Engineering

Program of Study Committee:
Rana Biswas, Co-major Professor
Vikram Dalal, Co-major Professor
Mani Mina

Iowa State University

Ames, Iowa

2009

# TABLE OF CONTENTS

# LIST OF TABLES

# LIST OF FIGURES

# ACKNOWLEDGEMENTS

I would like to take this opportunity to thank the many people that have helped me develop as a student and researcher. I thank my major professors, Vikram Dalal and Rana Biswas, for introducing me to research, sharing their knowledge, and supporting me throughout my graduate career. Their guidance and discussions greatly contributed to the success of this research. I also thank Mani Mina for serving on my committee.

I also thank Kay Han, Nayan Chakravarty, and Sambit Pattnaik for their helpful discussions and time spent making devices. Many thanks go to Max Noack for training me on all of the processing and characterization equipment, showing patience during the learning process, and frequently pointing me in the right direction. I would also like to thank Satya Saripalli and Ted Li for training me on device measurements, as well as Michael Eggleston for his assistance with this research.

I am very grateful for the friendship of past and present students at the Microelectronics Research Center, including Ryan Boesch, Jason Jirak, Brian Lewis, Aaron Thoeming, Atul Madhavan, Bob Mayer, Dan Stieler, Michael Beckman, Cole Petersburg, and Philip Reusswig.

I would also like to thank my family and friends for their constant support and encouragement over the years.

This research was supported by the NSF under grant ECCS-0824091, Iowa Powerfund, and Lightwave Power, Inc.

# ABSTRACT

Thin film hydrogenated amorphous silicon (a-Si:H) solar cells suffer from weak absorption of long wavelength photons, which have absorption lengths that are far greater than the absorber layer thickness. Light trapping schemes utilizing photonic crystal based back-reflectors can strongly diffract long wavelength photons and increase their optical path length. Photonic crystal back-reflectors were fabricated to investigate optical absorption enhancement in a-Si:H solar cells.

Photonic crystal back-reflectors were patterned with photolithography and etched in crystalline silicon wafers using reactive-ion etching. The etched photonic crystals were then coated with silver and aluminum doped zinc oxide for a highly reflective back contact. These structures had triangular lattice symmetry, an etch depth between 200 nm and 250 nm, and a pitch of 760 nm. Scanning electron microscopy images demonstrate high quality long-range periodicity. A-Si:H *n-i-p* solar cells were deposited on these back-reflectors using standard plasma enhanced chemical vapor deposition techniques.

Diffuse and total reflection measurements indicate high diffuse reflectance and strong absorption within the photonic crystal. Normalized external quantum efficiency (EQE) measurements demonstrated considerable absorption enhancement at near-infrared wavelengths. The photonic crystal back-reflector increased optical absorption by a factor of 6 to 7 at certain wavelengths, relative to flat reference devices on the same substrate. An enhancement of 8 times was also observed for a reference device on stainless steel coated with flat silver. Short circuit current, as determined by weighting EQE against the AM1.5 solar spectrum, increased by over 7% with the photonic crystal back-reflectors.

# CHAPTER 1. INTRODUCTION

## 1.1 Background

Global energy usage has increased exponentially and projections indicate that this trend will continue. Current energy demands are largely met with nonrenewable fossil fuels, including coal, oil, and natural gas [1]. Recent advances in extracting fossil fuels, such as heating oil shale, are generally expensive and environmentally detrimental. Renewable energy sources are naturally replenished and offer an alternative to fossil fuels. Solar radiation drives many terrestrial processes that have a large harvestable energy capacity, including air flow with wind turbines and photosynthesis with biomass. Solar radiation, in the form of optical wavelength photons, can also be converted to electrical current directly with photovoltaics. Photovoltaics, or solar cells, is an attractive field of renewable energy technology that continues to show significant growth as an energy source.

Solar cells are typically manufactured with silicon, an abundant semiconducting material that facilitates energy conversion. Despite this abundance, material costs and energy conversion efficiency have prevented solar cells from competing with fossil fuels. Monocrystalline silicon (c-Si) solar cells boast high efficiencies, but the need for expensive, high purity c-Si wafers have hindered their commercial growth. Thin film silicon solar cells consist of hydrogenated amorphous (a-Si:H) or nanocrystalline silicon (nc-Si:H), which is grown using chemical vapor deposition and silane gas. These solar cells use significantly less material, with the total device thickness ranging from 0.5 $\mu$m to 5

$\mu$m compared to c-Si wafers that are at least 300 $\mu$m thick. While thin film solar cells are cheaper to produce than c-Si solar cells, novel approaches to improve their efficiency are needed to make them competitive with nonrenewable energy sources.

## 1.2 Thin Film a-Si:H Solar Cells

Thin film a-Si:H solar cells consist of three unique layers that facilitate the absorption and transport of photogenerated carriers. Thin film solar cells are typically deposited on a substrate in an *n-i-p* configuration to achieve optimal transport properties within the device. In this structure, n-type a-SiC:H is closest to the substrate and functions as the electron transport layer. The intrinsic layer (i-layer) consists of a-Si:H and is where a majority of photons are absorbed. A p-type layer of a-Si:H is deposited on the i-layer to assist hole transport. An antireflective coating is deposited on the top of the p-type layer to minimize optical losses. Indium tin oxide (ITO) is also used as both an antireflective coating and top contact since it is both semi-transparent and conductive. This structure is shown in Figure 1.1.

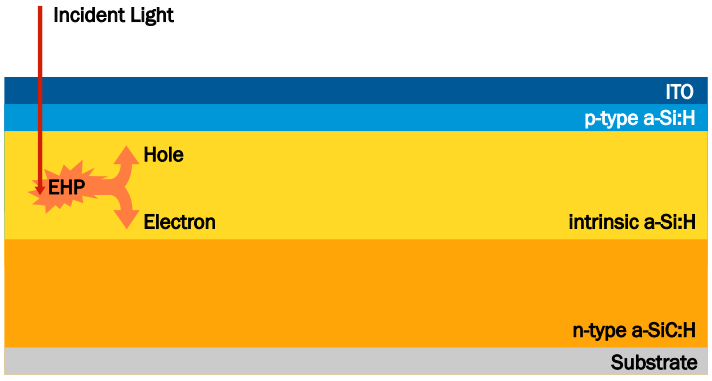


Figure 1.1 Device structure of an *n-i-p* a-Si:H thin film solar cell. Photon absorption and EHP generation is shown.

Solar cells are designed to maximize absorption within the i-layer and minimize recombination of generated carriers. Photons with energy greater than the bandgap of

a-Si:H [1] are ideally absorbed and generate an electron-hole pair (EHP) within the i-layer. An internal electric field across the i-layer causes the EHP to separate. The electron and hole then drift to the n-type and p-type layers respectively, where they are majority carriers and contribute to device current. Bulk recombination typically occurs when an EHP is generated within the n-type or p-type layers. The minority carrier will recombine immediately before it is able to drift across the i-layer. Absorption within the n-type layer is prevented by using a-SiC:H, which has a larger bandgap than a-Si:H. Surface recombination occurs at the a-Si:H/ITO and a-SiC:H/substrate interfaces, which also reduces current delivered by the solar cell.

## 1.3 Absorption Enhancement with Photonic Crystals

The i-layer thickness of a-Si:H solar cells is limited by several factors, including hole lifetimes and fill factor stability [2]. The probability that a hole recombines in the i-layer depends on mobility, lifetime, and the electric field across the i-layer. Thin i-layers not only have a larger electric field for a given applied voltage, but the amount of recombination decreases for shorter transit distances. The i-layer thickness for a-Si:H solar cells is typically 250 nm to 300 nm. Unfortunately, the probability that light is absorbed within the i-layer is also proportional to thickness. With an ideal back-reflector, this probability is given as:

$$P(\lambda) = 1 - \exp\left(\frac{-2t}{L_a(\lambda)}\right) \tag{1.1}$$

where $t$ is the i-layer thickness and $L_a(\lambda)$ is the wavelength dependent absorption length. For $2t >> L_a$, this equation approaches unity and all incident photons are absorbed. If $2t \leq L_a$ for photons with energy larger than the bandgap, significant absorption losses occur. The absorption length of a-Si:H is shown in Figure 1.2. Photons with wavelengths shorter than 550 nm have absorption lengths less than the i-layer thickness and are

[1] $E_{ph} > E_g$, which is approximately 1.75 eV for a-Si:H

effectively absorbed. However, the absorption length grows rapidly for wavelengths greater than 600 nm and exceeds 7 $\mu$m for photons near the band edge. Red and near-infrared photons are very difficult to absorb in thin a-Si:H layers.

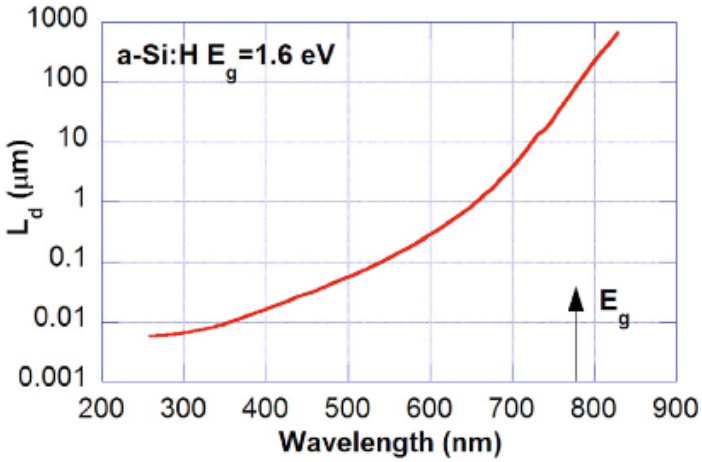


Figure 1.2 Absorption length of a typical a-Si:H solar cell for optical and near-infrared photon wavelengths [3].

Light trapping schemes are necessary for absorbing long wavelength photons in a-Si:H solar cells. One scheme that has shown promising simulation results utilizes a two-dimensional, metallic photonic crystal as a back-reflector. Two dimensional photonic crystals strongly diffract light at oblique angles over a range of wavelengths. When the diffraction angle is greater than the critical angle, total internal reflection causes photons to remain in the solar cell until they are absorbed. Standing waves within the cavities of the photonic crystal structure also contribute to absorption enhancement. An example of this back-reflector structure is shown in Figure 1.3(a).

The reflective properties of photonic crystals are determined by several geometric parameters, including the lattice symmetry, pitch ($a$), filling ratio ($R/a$), and etch depth. Optimizations were done with rigorous scattering matrix simulations, where Maxwell's equations were solved in Fourier space [3, 4]. Reflection and absorption were obtained

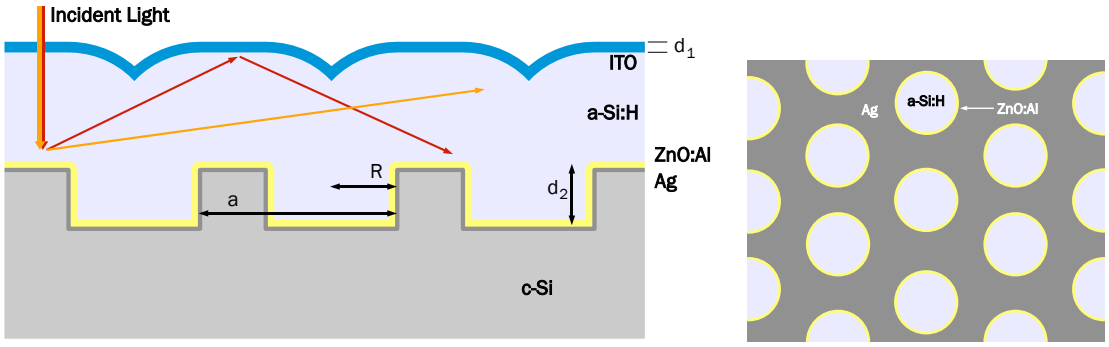


(a) (b)

Figure 1.3 Photonic crystal back-reflector device structure is shown in (a) and a cross section of the triangular lattice is shown in (b).

from the scattering matrix. Optimal simulated absorption occured for a triangular lattice photonic crystal with an etch depth ($d_2$) of 250 nm, filling ratio of 0.30, and pitch of 740 nm. These dimensions are shown in Figures 1.3(a) and 1.3(b). An a-Si:H thickness of 500 nm was also used. As shown in Figure 1.4, the simulated external quantum efficiency showed significant absorption of long wavelength photons for the photonic crystal back-reflector compared to a reference flat silver back-reflector. Absorption maxima between 650 nm and 780 nm are caused by diffraction resonances (standing waves) in the absorber layer, where optical path length and dwell time are enhanced [5, 6]. The electromagnetic fields are concentrated within the photonic crystal. There is little change in absorption below 600 nm since photons with absorption lengths less than the i-layer thickness are effectively absorbed before they reach the back surface. In this research, photonic crystal back-reflectors were fabricated to evaluate the absorption enhancement in a-Si:H solar cells.

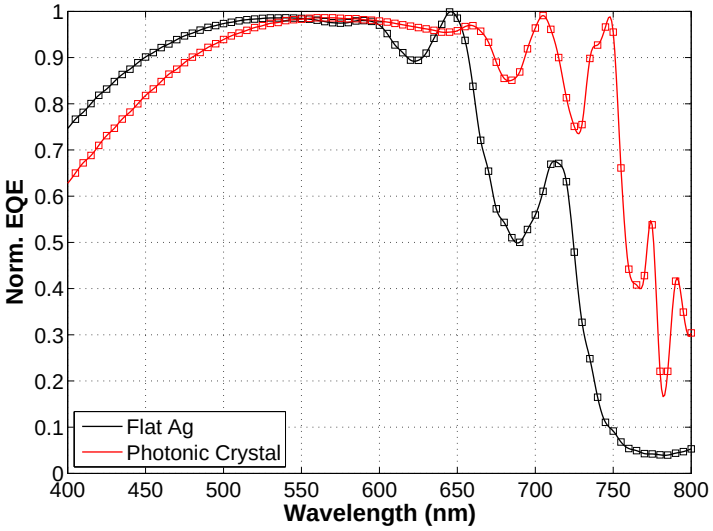


Figure 1.4 Simulated external quantum efficiency for an a-Si:H solar cell with a photonic crystal back-reflector and a flat Ag reference.

## 1.4 Literature Review

Light trapping and absorption enhancement schemes are major routes for improving thin-film solar cell efficiency. Research has focused on two methods: periodic structures based on photonic/plasmonic crystals and Lambertian surfaces that scatter light. One-dimensional photonic crystals have been used to achieve nearly 100% reflection over a broad range of wavelengths, as well as significant absorption enhancement when integrated with a diffraction grating or two-dimensional photonic crystal [7, 8, 3, 9]. Lambertian surfaces, such as etched ZnO, offer a relatively inexpensive method for improving absorption by scattering light [10, 11]. Results from textured polymer substrates are also presented, as this process would likely be used for roll-to-roll photonic crystal nano-imprinting [12].

### 1.4.1 Early Studies on Light Trapping

While there are many techniques to increase the internal light intensity within thin film solar cells, much of this work was preceded by early research on randomly roughened

surfaces. E. Yablonovitch and G. Cody argued that light incident on a textured slab will be internally scattered at random angles [13]. When a perfectly reflective (white) sheet is used on the back surface, the internal light intensity is larger than the incident intensity by a factor of $2n^2$, where $n$ is the wavelength-dependent refractive index of the slab. For an absorbing material, such as amorphous or crystalline silicon, the enhancement of internal light intensity was found to be $4n^2$ [13]. This serves as the theoretical limit for absorption enhancement in light trapping schemes. A study from 2003 stated that absorption can be enhanced by a factor of 10 in practice [14].

### 1.4.2 Textured 1-D Photonic Crystals

One-dimensional photonic crystals have been used in back-reflector designs due to their high reflectance, configurability, and lack of intrinsic plasmonic losses. By alternating two materials that have a large contrast in their refractive indices, 1-D photonic crystals can have nearly 100% reflectance around a central wavelength. When textured with a diffraction grating, solar cell absorption increases from strong diffraction modes, light trapping, and minimal reflection losses from the 1-D photonic crystal. These structures are also not subject to plasmonic losses, such as those seen in Ag back-reflectors coated with ZnO:Al at the rough metal-dielectric interface [15].

#### 1.4.2.1 Crystalline Si Solar Cells

Light trapping with a diffraction grating and 1-D photonic crystal in a c-Si solar cell was demonstrated by Zeng et al. [7]. Lateral *p-i-n* solar cells with interdigitated contacts were fabricated on the surface of a double-side polished 6 inch c-Si wafer. The rectangular diffraction grating, with grating period of 1.1 $\mu$m, was etched on the back of the wafer with projection lithography and plasma etching. The 1-D photonic crystal was then deposited on the grating with plasma enhanced chemical vapor deposition. Two different 1-D photonic crystals were investigated in this research: one with alternating

layers of Si and $Si_3N_4$ and the other with layers of Si and $SiO_2$. These structures had reflectances greater than 99.8% for wavelengths between 800 nm and 1100 nm.

As shown in Figure 1.5(a), external quantum efficiency was enhanced significantly with devices that had a 1-D photonic crystal and diffraction grating. For wavelengths greater than 1000 nm, the $Si/Si_3N_4$ 1-D photonic crystal and grating solar cell showed enhancement between 2 and 135 over a reference cell without a back-reflector structure. In addition to EQE, I-V measurements were performed to determine the increase in short circuit current and efficiency from the proposed back-reflectors. As shown in Figure 1.5(b), the solar cell with a $Si/Si_3N_4$ 1-D photonic crystal and grating had the highest short circuit current density. This increase in short circuit current density, 27.5 $mA/cm^2$ compared to 23.3 $mA/cm^2$ for the solar cell without a back-reflector, corresponded to an 19% increase in relative efficiency.

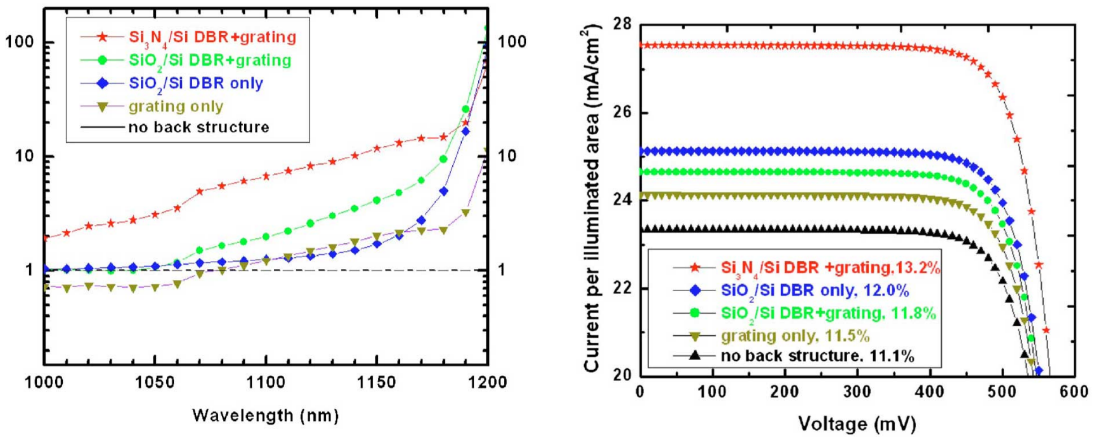


(a) (b)

Figure 1.5 External quantum efficiency enhancement factor for c-Si solar cells with different back-reflectors are shown in (a). I-V curves for these devices are shown in (b). Significant enhancement is shown for solar cells with a diffraction grating and DBR [7].

#### 1.4.2.2 Thin Film Monocrystalline Si Solar Cells

After increased absorption was shown for c-Si solar cells, Zeng et al. applied the same back-reflector concept to thin film, monocrystalline solar cells and found similar results [8]. The back-reflector was designed using couple wave theory and the scattering matrix method to obtain optimal reflection from the 1-D photonic crystal and large angle diffraction from the grating structure. These simulations resulted in a grating period of approximately 300 nm and an estimated 28.3% increase in short circuit current with respect to a flat reference cell. The solar cell was fabricated from an SOI wafer, which allowed for the back-reflector structure to be etched into the 5 $\mu$m thick active layer. The diffraction grating was patterned with interference lithography and reactive ion etching. Two variations of the 1-D photonic crystal were investigated: a flat structure that was achieved by chemical mechanical polishing and a wavy structure that followed the diffraction grating profile. The 1-D photonic crystal was deposited using plasma enhanced chemical vapor deposition. The thin active layer was transferred to a separate wafer, which exposed the unprocessed side and allowed for *p-i-n* solar cells to be formed with ion implantation.

In addition to the back-reflector structures with a grating and flat or wavy 1-D photonic crystal described above, a flat reference solar cell without a back-reflector and a solar cell with only a flat 1-D photonic crystal were fabricated as control samples. Simulated and experimental external quantum efficiency for these structures are shown in Figure 1.6(a). EQE was nearly identical for each solar cell at shorter wavelengths, but several shoulders can be observed for wavelengths greater than 640 nm. As expected, the reference had the lowest EQE relative to solar cells that utilized a textured photonic crystal back-reflector. The wavy 1-D photonic crystal and grating back-reflector solar cell had a short circuit current density of 17.45 mA/cm$^2$, which corresponded to a 18.9% increase over the flat reference cell. A slight drop in open circuit voltage was observed,

with 0.62 V for the wavy photonic crystal and grating solar cell compared to 0.65 V for the reference cell. This was thought to be caused by a larger reverse bias saturation current in the reference cell. I-V characteristics for these solar cells are shown in Figure 1.6(b). The overall relative efficiency increase was found to be 14.8%. The n-type and p-type implants on the top surface resulted in a poor reference device efficiency of 11.1%. Similar enhancement for more efficient devices is questionable.

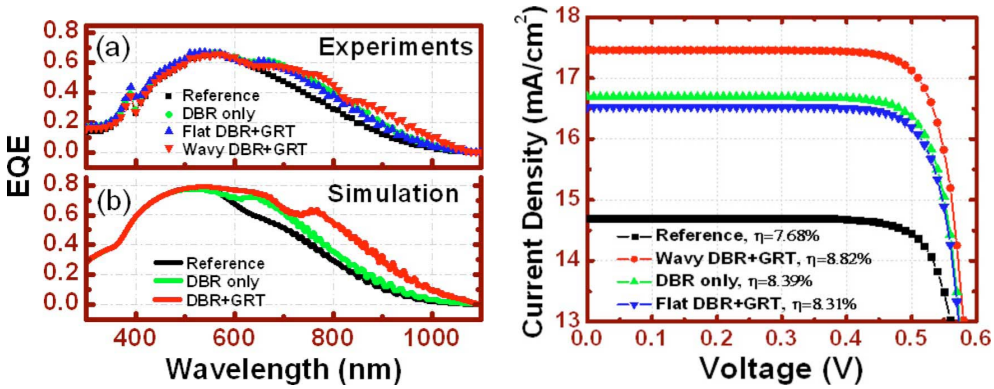


(a) (b)

Figure 1.6 Simulated and measured external quantum efficiency for monocrystalline thin film solar cells with different back-reflectors are shown in (a). I-V curves for these devices are shown in (b) [8].

### 1.4.3 Modulated 1-D Photonic Crystals

When used as a back-reflector for thin-film solar cells, 1-D photonic crystals typically suffer from a limited range of wavelengths with high reflectance. Krc et al. suggested modulating two different 1-D photonic crystals on glass to create an "ideal" back-reflector [9]. The photonic crystal consisted of alternating layers of n-type a-Si:H and ZnO:Al, which allowed it to be used as a back contact for the solar cell device. The first photonic crystal demonstrated high reflection at lower wavelengths (500 nm - 700 nm), while the second had similar behavior at higher wavelengths (700 nm - 1000 nm). These

wavelength ranges were optimized for a $\mu$c-Si solar cell with an i-layer thickness of 2 $\mu$m. Simulated internal reflectance from the rear part of the solar cell is shown in Figure 1.7.

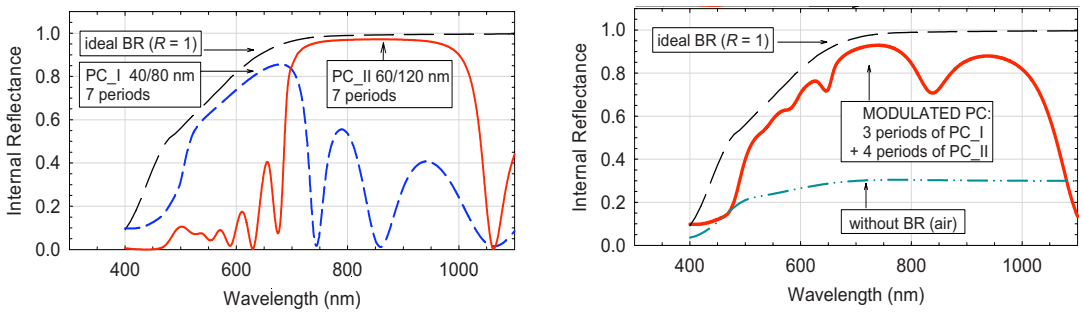


(a) (b)

Figure 1.7 Simulated internal reflectance of a $\mu$c-Si solar cell deposited on 1-D photonic crystals with layers of n-a-Si:H and ZnO:Al is shown in (a). Internal reflection of the modulated 1-D photonic crystal back-reflector is shown in (b) [9].

External quantum efficiency was simulated for a $\mu$c-Si solar cell on several different substrates: n-type a-Si:H back contact on glass, 1-D modulated photonic crystal as described above, and an ideal back-reflector with 100% reflection over all wavelengths. The results from these simulations are shown in Figure 1.8. As expected from the reflection data, the EQE for the modulated photonic crystal back-reflector was nearly identical to the ideal back-reflector. The improvement in short circuit current density from the proposed structure was over 13% when compared to the solar cell without a back-reflector. The modulated structure was shown to offer an additional 5% improvement in short circuit current density over each 1-D photonic crystal when they were used independently.

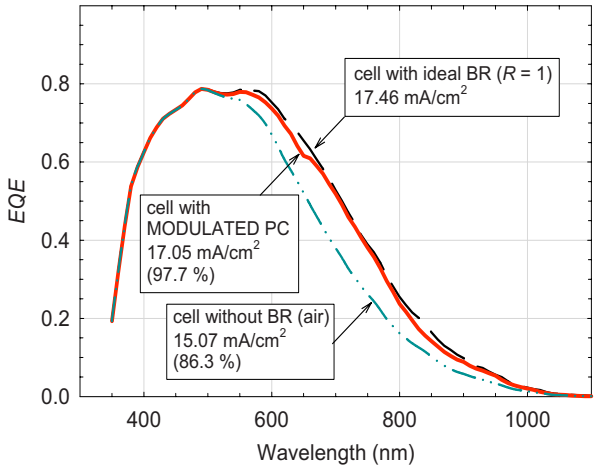


Figure 1.8 Simulated EQE for a $\mu$c-Si solar cell without a back-reflector, with the 1-D modulated photonic crystal back-reflector, and an ideal back-reflector [9].

### 1.4.4 Etched ZnO:Al

Etched ZnO:Al is a very effective and attractive method of scattering light within thin-film solar cells. When used as either the top contact in a superstrate or bottom contact in a substrate solar cell, etched ZnO:Al scatters incident light throughout the absorber layer over a wide range of wavelengths. Many thin film solar cell manufacturers are also capable of producing etched ZnO:Al substrates since the process requires an RF sputtering system and wet chemical etching with hydrochloric acid (HCl). Another advantage of this process is that the size and opening angle of the etched features are easily tuned by changing the total alumina concentration (TAC) in the ZnO sputtering target and substrate temperature during the ZnO:Al deposition [10]. The effect that these parameters have on etching is shown in Figure 1.9.

In addition to characterizing etched ZnO:Al for various deposition parameters, Berginski et al. deposited thin-film nc-Si solar cells on etched ZnO:Al superstrates [10]. In one series of etched ZnO:Al substrates, different substrate temperatures were used when sputtering ZnO:Al to achieve a variety of etched surfaces. The EQE for these devices

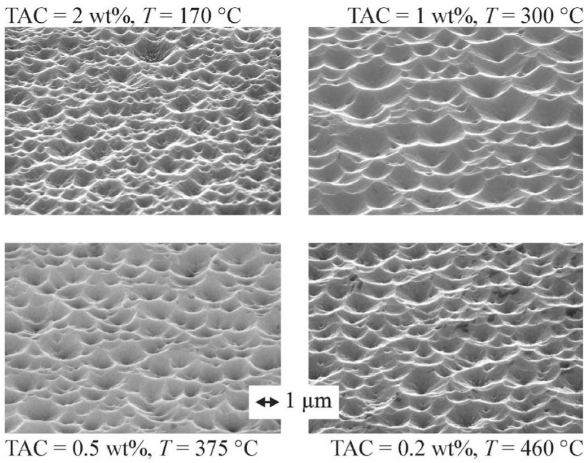


Figure 1.9 SEMs showing the effect of aluminum doping (0.2, 0.5, 1.0, and 2.0 wt%) and ZnO:Al sputtering temperature (170, 300, 375, and 460°C) on the etched features [10].

is shown in Figure 1.10(a). Significant absorption for wavelengths greater than 600 nm was observed with each substrate, but the highest (460°C) and lowest (290°C) substrate temperatures resulted in the greatest enhancement. Electrical performance and light trapping was found to be optimal with the 460°C substrate, since the lower temperature substrate required a voltage bias to assist carrier collection. The effect of etched ZnO:Al transparency and conductivity on solar cell efficiency was also studied. Solar cells with different i-layer thicknesses were deposited on etched ZnO:Al superstrates with 0.5 wt% and 1.0 wt% TAC. As shown in Figure 1.10(b), the EQE of 0.5 wt % TAC substrates resulted in the largest short circuit current for each i-layer thickness. A short circuit current of 26.8 mA/cm$^2$ was shown for a 1.9 $\mu$m thick i-layer, single junction device.

### 1.4.5 Textured Polymer Substrates

Polymer substrates, such as poly-ethylene-naphtalate (PEN), can be textured with photonic crystals and other periodic patterns to enhance absorption in thin-film solar cells. These substrates are relatively inexpensive, flexible, can be handled in a roll-to-

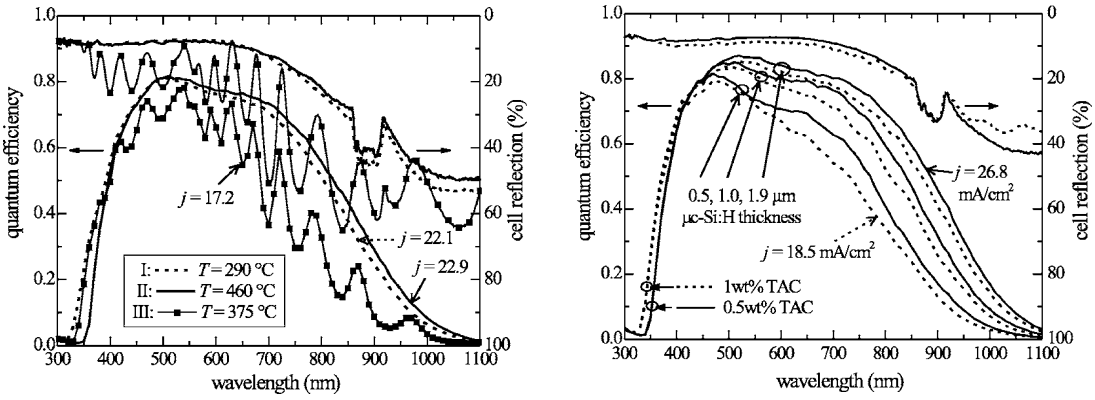


(a) (b)

Figure 1.10 EQE for $\mu$c-Si:H devices with varying substrate temperatures during etched ZnO:Al preparation is shown in (a). EQE for devices with different alumina ZnO doping is shown in (b), for both 1 wt% (dashed) and 0.5 wt% (solid) TAC. [10].

roll process, and are easily textured with nano-imprinting. Polymer substrates typically require low processing temperatures, which requires unique light trapping methods.

Haug et al. demonstrated enhanced absorption using textured PEN as the substrate for $\mu$c-Si devices [12]. The PEN substrate was periodically textured and coated with Cr, Ag, and ZnO. These films were deposited using a multi-source sputtering system that was capable of large-area coating. The *n-i-p* $\mu$c-Si solar cell was then deposited on the textured substrate using very high frequency plasma enhanced chemical vapor deposition. Boron doped ZnO was used as the top contact, and was deposited with low pressure CVD. A control sample with a flat Cr, Ag, and ZnO back-reflector on glass was also fabricated. The internal and external quantum efficiency of these devices device are shown in Figure 1.11. Considerable enhancement in EQE was shown for wavelengths greater than 700 nm, but the IQE showed possible plasmonic losses between 650 nm and 800 nm. Short circuit current density was improved by 27% with the textured substrate compared to the control solar cell, with currents of 22.8 mA/cm$^2$ and 17.9 mA/cm$^2$ respectively. A decrease in fill factor and open circuit voltage was also observed, but the

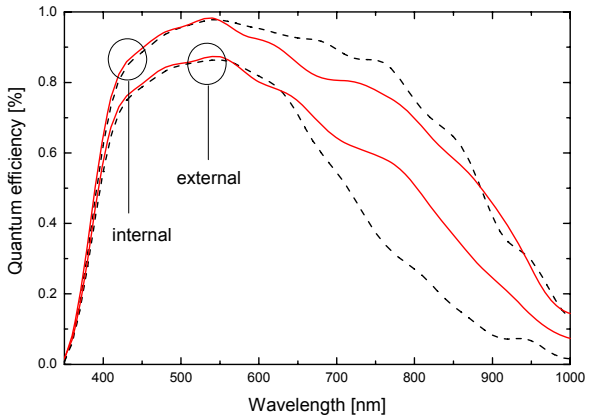


Figure 1.11 Internal and external QE for a thin film $\mu$c-Si solar cell deposited on textured poly-ethylene-naphtalate (solid) and a flat reference device (dashed) on Ag coated glass [12].

overall efficiency of increased with textured PEN substrates.

# CHAPTER 2. METHODOLOGY AND PROCEDURES

A process was developed to fabricate photonic crystal back-reflector substrates. The back-reflector solar cell devices consisted of a triangular lattice metallic photonic crystal, a-Si:H n-i-p solar cell device, and an ITO antireflective coating and top contact. The photonic crystal was etched into a patterned crystalline silicon wafer using reactive ion etching. Ag was then evaporated on the c-Si and used as both the back-reflector and back contact. A thin layer of ZnO:Al was sputtered on the Ag to prevent agglomeration during high temperature a-Si:H processing. The a-Si:H *n-i-p* solar cell was deposited using standard plasma enhanced chemical vapor deposition (PECVD) techniques. A thin ITO top contact and antireflection coating was sputtered on the surface to complete the solar cell device.

## 2.1 Photonic Crystal Back-reflector Fabrication

### 2.1.1 Photolithography

Six inch crystalline silicon wafers were used as the bulk photonic crystal structure. The minimum feature size of the photonic crystal was approximately 300 nm, as defined by the spacing between etched c-Si cylinders. An ASML 193 nm step-and-repeat aligner was used to expose the photoresist with enough resolution to achieve the optimal dimensions. The 12mm by 12mm photonic crystal pattern was exposed into 500 nm of Rohm and Haas Epic 2135 photoresist and 80 nm of a bottom antireflective coating (BARC). Since photoresist was the etch mask in this process, a sufficiently thick layer

was required for reactive-ion etching.

### 2.1.2 Substrate Preparation

Once the wafers were patterned, a stainless steel scribe was used to split the wafer into eight, 36 mm by 36 mm substrates. Each substrate was cleaned with $N_2$ to remove c-Si debris introduced when the wafer was scribed. The substrates were then placed in single wafer carriers. The substrate dimensions were defined by substrate holders and masks used in processing tools that were used in this research. The photonic crystal was positioned on the substrate to allow for a flat a-Si:H device that was used as a reference.

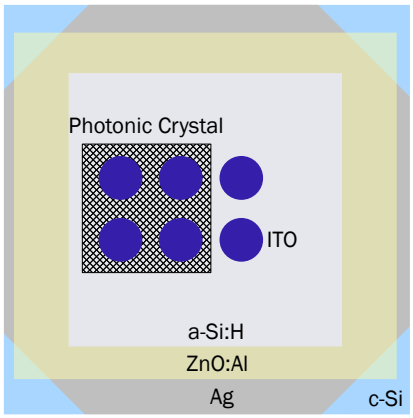


Figure 2.1 Layout of the photonic crystal back-reflector substrate. ITO contacts define the a-Si:H devices.

### 2.1.3 Reactive Ion Etching

A PlasmaTherm 700 series reactive-ion etching (RIE) system was used to etch the patterned wafers. Although wet etching is often highly selective and does not require a vacuum system, dry etching offers greater anisotropy and reproducibility. Dry etching also has several disadvantages, including the deposition of a residue that remains on

surfaces during the etching process and the etch rate profile across the electrode. Despite these limitations, dry etching with an RIE offers consistent etch depths and well-defined features which are critical when fabricating optical wavelength photonic structures.

Crystalline silicon was etched with a carbon tetrafluoride ($CF_4$ or Freon 14) and oxygen plasma. $CF_4$ is an inert gas that can be easily dissociated with an RF plasma to produce fluorine radicals. Atomic fluorine bonds with exposed silicon to form silicon tetrafluoride ($SiF_4$), which is then desorbed from the silicon surface. This reaction is shown below:

$$CF_4 + e^- \rightarrow CF_3 + F + e^- \tag{2.1}$$

$$Si + 4F \rightarrow SiF_4 \tag{2.2}$$

Additional complex and undesirable reactions occur when etching with $CF_4$. Carbon and fluorine can recombine and form a C-F polymer on surfaces within the etching chamber [16]. This polymer is difficult to remove and inhibits etching. $CF_4$ is also effective at etching polymers, such as photoresist and the BARC.

The addition of $O_2$ further increases the fluorine concentration in the plasma by combining with carbon. This relationship is well documented and a maximum fluorine concentration occurs with approximately 12.5% $O_2$ [17]. While the silicon etch rate increases with increased fluorine concentrations, an excessive amount of $O_2$ reduces the etch rate as the silicon surface is oxidized [18].

Several objectives were defined when testing the various RIE parameters, which are listed in Table 2.1. Due to the relatively thin organic-based etch mask, obtaining the greatest etch selectivity between c-Si and photoresist was critical. The third set of parameters yielded the best selectivity of 1.32 for photoresist to c-Si etching. Etch anisotropy was also needed since the simulated structure used side-walls that were orthogonal to the c-Si surface. While this was not measured quantitatively, SEMs indicated that the third recipe also had the best anisotropy. Minimizing C-F polymer formation

on the surface was also investigated and is discussed in the appendix.

Table 2.1 RIE etch process parameters

| Recipe | $CF_4$ (sccm) | $O_2$ (sccm) | RF Power (W) | DC Bias (V) | Pressure (mTorr) |
|---|---|---|---|---|---|
| 1 | 58 | 5 | 31 | 127 | 25 |
| 2 | 80 | 5 | 47 | 127 | 50 |
| 3 | 50 | 6 | 51 | 127 | 50 |

Photoresist etch rates were determined with a Nanospec spectrophotometer by measuring thickness based on refractive index, reflection maxima and minima from optical interference, and reflection intensity. A combination of side-profile SEMs and profilometer scans were used to measure the c-Si etch rate. The etch rate and selectivity for each set of process parameters is shown in Table 2.2.

Table 2.2 Etch rates for the tested process parameters

| Recipe | c-Si ($nm \cdot min^{-1}$) | PR ($nm \cdot min^{-1}$) | Selectivity (PR/c-Si) |
|---|---|---|---|
| 1 | 8 | 22 | 2.75 |
| 2 | 17 | 30 | 1.76 |
| 3 | 22 | 29 | 1.32 |

### 2.1.4 Substrate Cleaning

After etching the photonic crystal pattern with $CF_4$ and $O_2$, the remaining photoresist and bottom anti-reflection coating was stripped by an additional plasma etch with $O_2$. In addition to the convenience of removing these layers without wet processing steps, it was found that the BARC layer did not react with acetone.

Several $O_2$ plasma parameters were tested to determine which process was most effective at cleaning the surface. The parameters for each process can be found in Table 2.3. Each set of parameters was capable of completely removing the photoresist and BARC layers. The higher power plasma appeared to reduce particulates on the surface

introduced during the etching and cleaning steps. Earlier runs used the lower power process, while substrates processed towards the end of this research were cleaned with the high power process. The total duration was determined by the particulate density on the c-Si surface after an initial 5 minutes of $O_2$ plasma cleaning. In general, 5 minutes to 10 minutes was sufficient and additional time did not yield a cleaner surface.

Table 2.3 Oxygen plasma cleaning process parameters

| $O_2$ (sccm) | RF Power (W) | DC Bias (V) | Pressure (mTorr) | ER ($nm \cdot min^{-1}$) |
|---|---|---|---|---|
| 10 | 50 | 172 | 50 | 75 |
| 50 | 150 | 292 | 98.6 | 210 |

### 2.1.5 Silver Thermal Evaporation

Once the c-Si sample was etched and cleaned, Ag was thermally evaporated on the substrate. Ag was chosen due to its high specular reflectance at red and near-infrared wavelengths and low sheet resistance. As shown in Figure 2.2, Ag total reflectance is above 90% for light with wavelengths greater than 500 nm. Plasmonic losses cause the reflectance to decrease for shorter wavelengths, but these losses occur where back-reflectors are mostly ineffective in a-Si:H solar cells.

In thermal evaporation, Ag particles ballistically travel from the source to the substrate. These particles can be blocked, or shadowed, by features on the substrate. This property results in non-uniform depositions on textured substrates, as the thickness on vertical features will be significantly less than the amount deposited on flat surfaces. Therefore, a sufficiently thick layer of Ag is needed to ensure adequate side-wall coverage.

Before evaporating Ag on the photonic crystal substrate, the bell-shaped, vertical enclosure was brought to vacuum. With the substrate on a stage and facing the metal targets, the enclosure was lowered and held flush against the base of the evaporator. A

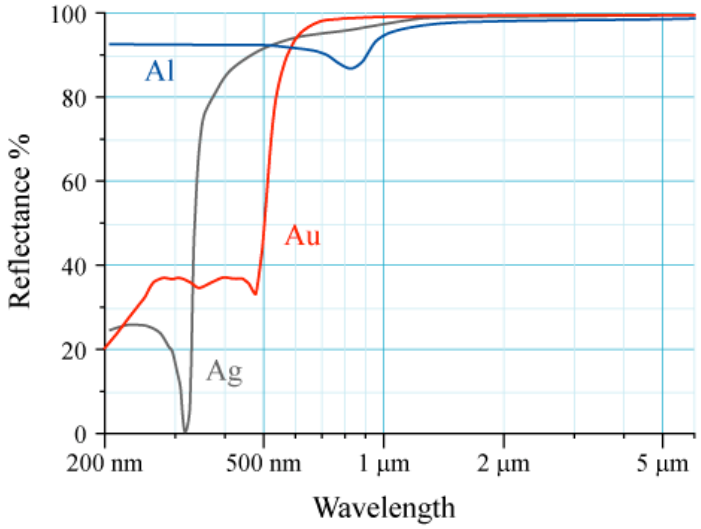


Figure 2.2 Total reflectance for aluminum, gold, and silver mirrors [19].

roughing pump valve was opened to bring the chamber pressure down to approximately 1 Torr. Several nitrogen ($N_2$) purges are usually necessary to reduce the amount of water vapor within the chamber. This was done by closing the roughing pump valve, flowing $N_2$ into the chamber for 15 seconds, and then opening the roughing pump valve to reduce the pressure. After purging and once the chamber is at 1 Torr, the roughing pump valve was closed before the opening turbo gate valve to bring the pressure down further. Several 5 second purge cycles were performed after the chamber pressure is reduced with the turbo pump. After purging, the turbo gate valve was opened after roughing out the chamber and an ion pressure gauge was used to determine the chamber pressure. Pressures were typically on the order of $1 \times 10^{-6}$ Torr.

After the chamber pressure was below $1 \times 10^{-6}$ Torr, the evaporator was configured to deposit Ag. A Maxtek TM200R thickness monitor was initialized by selecting the appropriate acoustic impedance and density of Ag. The thickness monitor was connected to a crystal oscillator located inside the evaporator and gave a real-time measure of thickness from changes in oscillation frequency during the deposition. A shutter, placed between the sample and metal source, was also closed before the metal was de-gassed.

De-gassing was performed by slowly increasing the current to the tungsten boat or rod until it was just below the evaporation point of the metal. Through joule heating, the temperature of the tungsten boat and Ag increased with current and caused various compounds to evaporate. This process initially caused an increase in chamber pressure as impurities evaporate, but the pressure eventually decreased once the metal was adequately de-gassed.

Once the thickness monitor was set and the source metal was de-gassed, Ag was evaporated on the substrate. The current was increased until the thickness monitor indicated a sufficient evaporation rate, which was typically 5 $\mathring{A}$/s to 10 $\mathring{A}$/s. The shutter was then opened and the thickness monitor was set to display the total evaporated thickness. After the desired thickness was evaporated, the shutter was closed and current was decreased. The substrate was then ready for ZnO:Al sputtering.

### 2.1.6 ZnO:Al Sputtering

ZnO:Al was sputtered to prevent the silver from agglomerating during the a-Si:H device deposition, which was typically performed at 300°C to 350°C. Agglomeration occurs at high temperatures, where Ag films form voids, hillocks, and islands to reduce the total energy of the system[1] [20, 21]. A low temperature ZnO:Al deposition was also needed to prevent agglomeration during the sputtering process.

The samples were first loaded into a sputtering chamber that contained ITO and ZnO:Al sputtering targets. Similar to the metal evaporation process, a roughing pump was used to bring the chamber to a relatively low pressure of 1 Torr. Several $N_2$ purges were done by flushing the chamber with $N_2$ for 30 seconds and then bringing the pressure back to 1 Torr with the roughing pump. With the chamber at 1 Torr, the turbo gate valve was opened to bring the chamber to lower pressures. The chamber was then purged several times by flowing $N_2$ for 15 seconds after closing the turbo gate valve and then

[1] This is particularly true with partial pressures of $O_2$

pumping the chamber out with the roughing and turbo vacuum pumps. This typically resulted in a base pressure of approximately $1 \times 10^{-6}$ Torr.

Once the chamber reaches a sufficiently low base pressure, the substrate heater controller was set to 150°C. Once the temperature gauge displayed the desired temperature, the chamber pressure was brought to 10 mTorr by flowing 100% argon into the chamber and adjusting the turbo gate valve. After the pressure stabilized, an RF power supply was turned on and set to 40 W. The ZnO:Al sputtering target and plasma were allowed to condition with the shutter closed for several minutes. The shutter was then opened to expose the substrate and deposit ZnO:Al.

## 2.2 a-Si:H Device Fabrication

### 2.2.1 Plasma-enhanced Chemical Vapor Deposition

Amorphous silicon *n-i-p* solar cells were deposited on the photonic crystal substrates using plasma enhanced chemical vapor deposition (PECVD). The various a-Si:H layers are deposited on the substrate by applying an RF signal between two electrodes and flowing precursor gases that dissociate in a plasma. The substrate is grounded and faces an electrode that is supplied with a high power RF signal. The various precursor gases used to form the device layers included phosphine ($PH_3$) for n-type doping, diborane ($B_2H_6$) for p-type doping, silane ($SiH_4$) for intrinsic a-Si:H, and methane ($CH_4$) to react with silane and form amorphous silicon carbide [22].

The solar cell device was deposited in a single reactor, which is shown in Figure 2.3. The substrate was placed on the substrate holder, which was loaded and unloaded from the top of the reactor and contained a heating element to adjust the substrate temperature. A grounded shutter was placed between the area of the substrate holder that contained the device and the RF electrode. By adjusting the position of the shutter, the sample was either exposed or isolated from the plasma. The RF electrode was

connected to an external impedance matching apparatus. A function generator and power amplifier supplied the RF signal to the impedance matching unit, which was tuned to minimize the reflected RF power. Intrinsic and dopant gas lines were isolated and separately controlled, which reduced contamination in the i-layer by allowing for parasitic gases within the dopant lines and chamber to be purged.

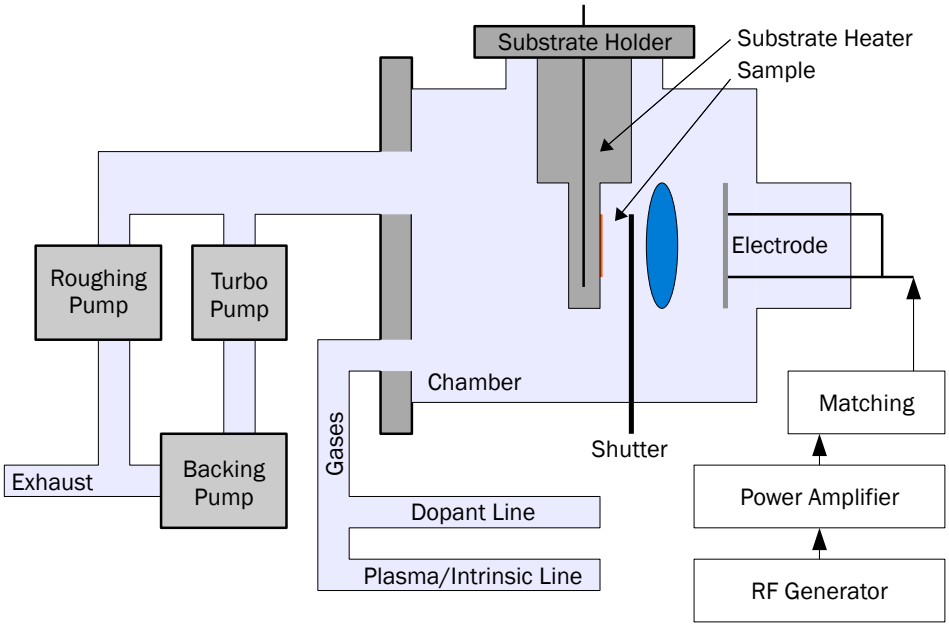


Figure 2.3 Diagram of the plasma enhanced chemical vapor deposition reactor used to deposit a-Si:H devices.

The photonic crystal substrates were first loaded onto the substrate holder. The substrate holder was then placed in the designated opening on top of the chamber. A roughing pump was used to bring the chamber to 1 Torr, which was followed by opening the turbo pump valve to achieve a chamber pressure less than $1 \times 10^{-6}$ Torr. Once the chamber reached the desired base pressure, the substrate heater was set to 300°C and allowed time to stabilize. The intrinsic and dopant gas lines were enabled and silane, phosphine, and methane mass flow controllers (MFCs) were adjusted and set to flow. The turbo gate valve was then adjusted to regulate the chamber pressure and an RF

signal was applied to the electrode to form the plasma. Silane, phosphine, and methane dissociate in the plasma and form free radicals, which are ultimately deposited on the surface to form n-type a-SiC:H. The deposition time was set to achieve a 250 nm film thickness with calibrated growth rates. This thickness was chosen to prevent shorts during testing. The RF signal was then disabled to allow for the chamber and gas lines to be purged before the i-layer deposition. With the chamber purged, silane was set to flow into the reactor and the RF signal was applied to the electrode. Intrinsic a-Si:H was then deposited on the n-type layer until the desired thickness was reached. The i-layer thickness was typically between 250 nm to 300 nm. The thin p-type layer was then deposited by flowing silane and diborane into the chamber, which dissociate to form p-type a-Si:H. This layer was approximately 10 nm thick, since electron-hole pairs generated in this film do not generally contribute to current delivered by the solar cell. After the device deposition was finished, the reactor was purged and the substrate holder was given time to cool before it was removed.

### 2.2.2 ITO Sputtering

ITO was sputtered on the p-layer of the a-Si:H device to form the top contact. ITO is commonly used as a contact since it is fairly transparent and conductive. The thickness of the ITO layer was set to 70 nm, which allowed it to serve as both a contact and antireflection coating.

The ITO contacts were deposited in the same sputtering chamber as ZnO:Al. Similar to the previous steps, a low chamber background pressure was reached with the roughing pump, turbo pump, and an adequate number of purges. Once the chamber reached $1 \times 10^{-6}$ Torr, the substrate heater was set to 225°C. After the substrate stabilized at the set temperature, argon and oxygen gas flows were introduced to the chamber and the chamber pressure was set to 5 mTorr by adjusting the turbo gate valve. With the shutter closed, the DC power supply was turned on and set to 20 W. This was

sustained for several minutes to condition the ITO sputtering target and DC plasma. After conditioning, the shutter was opened to begin the 2.5 minute deposition.

# CHAPTER 3. CHARACTERIZATION

The photonic crystal back-reflector substrates and a-Si:H devices were characterized to evaluate substrate processing and reflective properties, as well as device performance. In this section, characterization techniques and device measurements are discussed.

## 3.1 Photonic Crystal Back-reflector Substrates

Throughout the entire photonic crystal back-reflector fabrication process, certain characterization steps were utilized to verify the structural integrity and optical performance. Scanning electron microscopy (SEM) was used to inspect the samples after each processing step and evaluate the effects of various process changes. SEMs were typically taken after RIE etching and $O_2$ plasma cleaning, Ag evaporation, ZnO:Al sputtering, and ITO sputtering. Diffuse and total reflection measurements were also performed after Ag was evaporated and ZnO:Al was sputtered.

### 3.1.1 Scanning Electron Microscopy

A Jeol 6100 scanning electron microscope was used to image the photonic crystal back-reflectors. The SEM had attachments for both secondary electron and back-scattered electron detection. The secondary electron detector was used due to its greater resolution and ease of operation. The SEM was controlled through a central console that contained standard adjustment dials and a display to both preview the scan and view a histogram from the rasterizing beam. A computer was also configured to interface with

the SEM and control the scanning parameters. Through numerous scans, it was found that the SEM could resolve features on the order of 10 nm when the sample was scanned slowly with significant averaging to reduce noise.

Imaging the substrate with an SEM was a significant portion of substrate characterization. Due to a large contrast in conductivity between some of the materials used to process the back-reflectors, a simplistic form of surface analysis was possible. This was particularly important when determining whether the photoresist and BARC was adequately removed, since these materials would "charge" in the SEM and appear embossed once rasterized by the scanning beam. Figure 3.1(a) shows an example of the embossing seen in organic materials. The scanning beam would also typically leave a carbon based residue on the substrate, and this residue was more apparent on conductive materials such as c-Si and metal.

The SEM was also capable of measuring the etched photonic crystal geometries on the substrates. Once a particular area was scanned and saved, markers were placed throughout the pattern to determine the pitch, radius, and etch depth. While pitch and radius were determined with images of the photonic crystal surface, the etch depth could only be accurately determined when the scanning beam was in-plane with the c-Si substrate. For etch depth measurements, the c-Si substrate was split along the crystal plane and through the photonic crystal pattern. The split substrate was then placed vertically in the SEM, with the photonic crystal region of the substrate facing the scanning beam. An example of measurements performed with the SEM can be seen in Figure 3.1(b).

### 3.1.2 UV-Vis-NIR Spectroscopy

Diffuse and total reflection measurements were performed with an Ocean Optics HR4000 spectrometer and an ISP-REF integrating sphere. A tungsten-halogen light

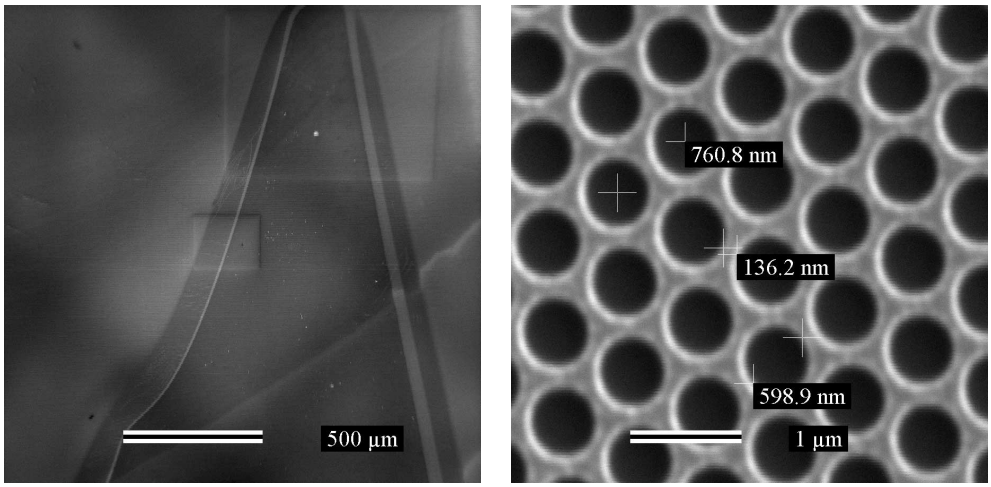


(a) (b)

Figure 3.1 Examples of SEM characterization on a 750 nm pitch photonic crystal substrate. The organic embossing effect is shown in (a) and measurement capabilities are shown in (b).

source was built into the integrating sphere and directed light towards an aperture located at the top of the unit. The light source was rated at 3100 K, which has a spectral illumination range of 360 nm to 1000 nm. The inside of the integrating sphere was coated with Spectralon, a highly Lambertian reflecting surface rated for over 98% diffuse reflectivity between 400 nm and 1500 nm. The integrating sphere contained two additional apertures: one for measuring the light intensity with an external spectrometer using an optical fiber and another that could be toggled to include or exclude specular reflectance. When the second aperture was opened, a "black" surface was exposed to prevent the specular component of reflection from being scattered (and measured) within the integrating sphere. The result was a measure of diffuse reflectance. Total reflectance was measured by closing the aperture, which covered the black area with the same highly diffuse surface used throughout the integrating sphere. This modification caused the specular component to be scattered and included in the reflectance measurement.

The ability to take reliable diffuse and total reflection measurements was largely dependent on the recorded baselines. Before the sample was measured, a diffuse reflection

standard with nearly 99% reflectance was placed on the top aperture. The signal integration time and averaging was modified to ensure that the spectrum peak did not saturate the spectrometer photodetectors while maintaining a strong signal. Electrical correction was also enabled, which read the signal from outlying detectors and subtracted this "noise" from the entire spectrum. A 100% baseline was then recorded. The 0% baseline was found after the diffuse reflection standard was replaced with a container lined with black insulating foam. The black lining ensured that the fluorescent light spectrum would not confound the baseline. This calibration was performed before substrates were measured as well as after switching between diffuse and total reflection.

## 3.2 a-Si:H Devices

After a-Si:H devices were deposited on the photonic crystal substrates, they were characterized with several different measurements. Current-voltage (I-V) measurements were performed while the device was illuminated to determine typical solar cell parameters, such as short-circuit current, open circuit voltage, and fill factor. External quantum efficiency (EQE) was also measured for a quantitative assessment of absorption within the solar cell at specific wavelengths of light.

### 3.2.1 Current-voltage Measurements

Current-voltage (I-V) measurements were taken immediately after the top contacts were sputtered. The I-V measurement apparatus consisted of an ELH bulb connected to an AC power supply with a voltage transformer. The ELH bulb was suspended at a fixed height above a black stage. Two probes were positioned directly beneath the light source and connected to a voltage supply. A fan was also placed near the probes to reduce the effect of heat from the ELH bulb when devices were measured.

The device was first placed on a glass slide to isolate it from the test bench. The ELH

light source was then switched on and current delivered to the bulb was increased until the transformer indicated that it was voltage-limited. The probes were then placed on the top and bottom contact to apply a range of bias voltages while measuring current. This process was automated with a computer interface that controls both the voltage supply and ammeter.

The ELH bulb had an emission spectra that resembles the standard AM1.5 solar spectrum at a specific voltage. The power supply was set to 120 V to minimize variation between the emitted and true solar spectrum. As shown in Figure 3.2, the ELH emission appears to be weighted towards red and infrared wavelengths when compared with the AM1.5 spectrum.

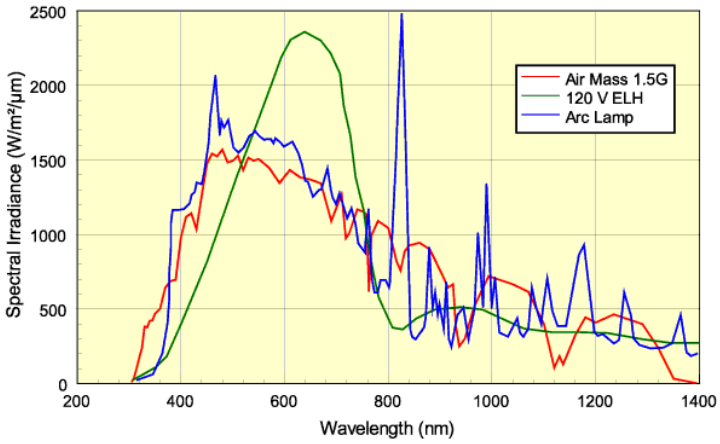


Figure 3.2 The standard AM1.5 spectrum compared with the spectrum from an ELH bulb and arc lamp [23].

The main objective of measuring I-V characteristics was to determine the quality of the solar cell device when illuminated. Quality was measured with the following parameters: short circuit current density ($J_{sc}$), open circuit voltage ($V_{oc}$), fill factor ($f.f.$), and efficiency ($\eta$). Short circuit current density is defined as the current per unit area that the solar cell generates when there is zero applied voltage between the device contacts. The voltage that causes the solar cell to behave like an open circuit, or deliver

zero current, is referred to as the open circuit voltage. Open circuit voltage largely depends on the photo-generated ($I_L$) and reverse saturation ($I_0$) currents, as shown in the following equation [24]:

$$V_{oc} = \frac{kT}{q} \ln\left(\frac{I_L}{I_0} - 1\right) \tag{3.1}$$

where $k$ is Boltzmann's constant, $T$ is temperature in Kelvin, and $q$ is the charge of an electron. Fill factor was found by determining the voltage ($V_m$) and current ($I_m$) that delivers maximum power and taking the following ratio [24]:

$$f.f. = \frac{I_m V_m}{I_{sc} V_{oc}} \tag{3.2}$$

Efficiency is defined as the ratio of the maximum power generated by the solar cell under AM1.5 illumination to the total power incident on the surface, as defined by the AM1.5 spectrum. The standard measure for total AM1.5 power density is 100 mW/cm$^2$. Solar cell efficiency can be expressed as the following:

$$\eta = \frac{P_{max}}{P_{AM1.5}} = \frac{J_{sc} V_{oc} f.f.}{100\ mW/cm^2} \tag{3.3}$$

Although fill factor and efficiency are the most common figures of merit when designing solar cells, back-reflector research typically focuses on improvements in short-circuit current density.

Shunt and series resistance were also extracted from the solar cell I-V characteristics. These resistances account for parasitics within the device, including low resistive paths through the i-layer and contact resistance. Shunt resistance was calculated from the inverse slope of the I-V curve when a negative bias is applied to the solar cell. Series resistance was found from the inverse slope for positive applied voltages. The slopes used to determine shunt and series resistance for a typical a-Si:H device are shown in Figure 3.3.

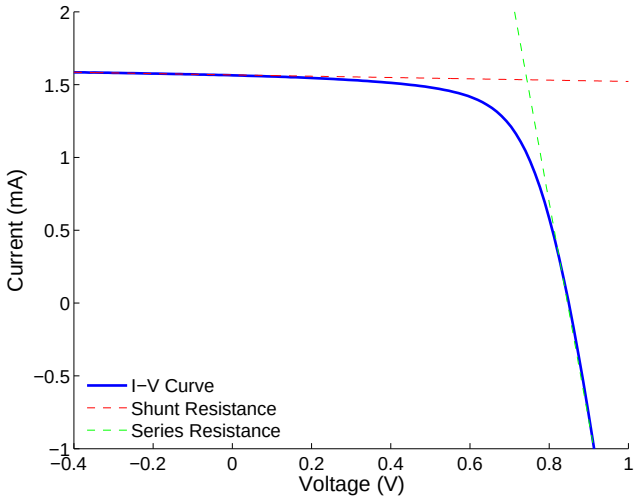


Figure 3.3 I-V relationship for an a-Si:H solar cell device. Series resistance is determined by the inverse slope of I-V under positive bias (green) and shunt resistance is the inverse slope of negative bias I-V (red).

### 3.2.2 External Quantum Efficiency

External quantum efficiency (EQE) was measured to determine wavelength dependent collection within the a-Si:H solar cell. EQE is a quantity defined as the number of electrons obtained outside of the device divided by the number of incident photons. The EQE measurement apparatus used a light source that was channeled into a single-grating monochromator to select a specific wavelength. Since the light output from the monochromator contained several diffraction modes, various optical filters[1] were placed in the optic path to block unwanted modes. Light from the monochromator passed through a chopper which rotated at 13 Hz. A transresistive pre-amplifier was used to convert device current to voltage and was attached to the sample probes. The chopper and output of the pre-amplifier were connected to a Stanford Research Systems SR830 digital lock-in amplifier, which integrated the output signal from the pre-amplifier and

[1] 800 nm - 700 nm: 700 nm high-pass filter, 700 nm - 580 nm: No filter, 580 nm - 400 nm: "Hot-glass" band-pass filter

the reference signal from the chopper. This setup was ideal for measuring small signals since readings that were out of phase with the chopper were effectively eliminated from the signal reading. A diagram of this setup is shown in Figure 3.4.

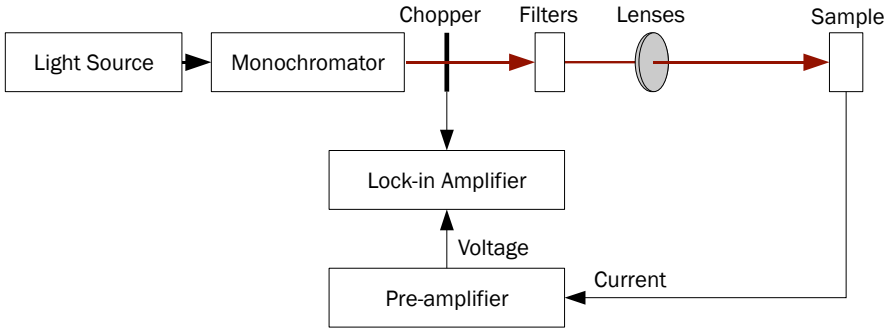


Figure 3.4 Diagram of the external quantum efficiency apparatus.

EQE was determined from lock-in amplifier voltage readings for an a-Si:H solar cell and a reference c-Si photodiode with a known absolute quantum efficiency. EQE was calculated with:

$$EQE = EQE_{ref}\left(\frac{V_{device}}{V_{ref}}\right) \tag{3.4}$$

for measurements that were taken from 400 nm to 800 nm in 20 nm increments. This measurement is not absolute due to unknown differences in light intensity and illumination area between the device and photodiode. Therefore, the EQE for all devices is normalized to 90%. The validity of this assumption greatly depends on the peak EQE of the a-Si:H device, since the absolute EQE of the photodiode is approximately 90% near the a-Si:H device EQE maxima.

An estimate of the solar cell short circuit current was also found by summing the product of device quantum efficiency and AMI 1.5 current at each measured wavelength. This was calculated with:

$$J_{sc,EQE} = \sum_{\lambda=400nm}^{800nm} q\,\Phi(\lambda)\,EQE(\lambda) \tag{3.5}$$

where $q$ is the unit charge of an electron, $\Phi(\lambda)$ is the AM1.5 solar flux in photons/sec/cm$^2$, and $EQE(\lambda)$ is the measured EQE at a specific wavelength.

# CHAPTER 4. RESULTS AND DISCUSSION

## 4.1 Photonic Crystal Back-reflector Substrates

In this section, each of the processing steps used to fabricate the photonic crystal back-reflectors is discussed. After reactive-ion etching and $O_2$ plasma cleaning, SEMs were used to determine the cleanliness of the substrate and lattice dimensions. SEMs were also taken after Ag evaporations and ZnO:Al sputtering to improve the process by identifying parameters that minimized Ag agglomeration. Diffuse and total reflectance were used to determine the optical characteristics of the photonic crystal.

### 4.1.1 Etched c-Si

Substrates were etched with each of the $CF_4/O_2$ plasma parameters discussed in Section 2.1.3. Since the selectivity was improved with each set of parameters, the etching time was set to etch between 200 nm and 250 nm while retaining a layer of photoresist and BARC to avoid etching the masked c-Si surface.

As shown in Figure 4.1, the photonic crystal lattice was successfully etched into the c-Si substrate. The photoresist and BARC layers were etched off the surface and polymer formation on the side-walls of photonic crystal was not observed. Etched features appeared to be uniform in the scanned area and across the substrate, indicating long-range order in the photonic crystal pattern. Although it is not evident in the SEM, the substrates did not show signs of large particle contamination or defects that were greater than the photonic crystal pitch. Small particles, typically 100 nm in diameter,

were also observed on the entire substrate. Additional comments and an alternative cleaning procedure can be found in the appendix.

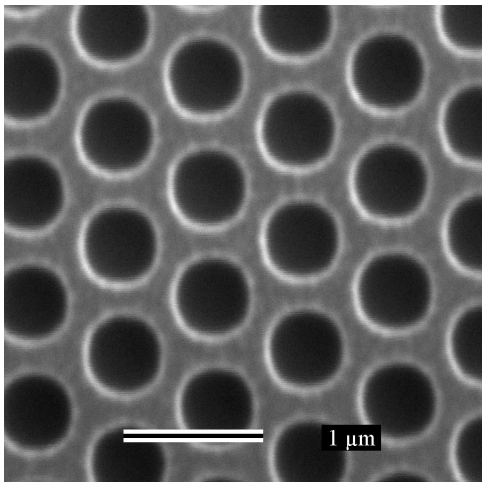


Figure 4.1 SEM of the c-Si photonic crystal back-reflector after RIE etching and $O_2$ plasma cleaning. (25,000x magnification and 1$\mu$m scale)

The photonic crystal lattice was measured for substrates etched with each set of plasma parameters. These measurements are provided in Table 4.1. Since $CF_4$ is not an anisotropic etchant for c-Si, side-wall etching resulted in a larger photonic crystal diameter than intended and increased the filling ratio ($R/a$). Side-wall etching was compensated with subsequent Ag and ZnO:Al depositions and reduced with modifications to the etching plasma parameters. The lattice pitch was also consistently measured to be 760 nm, which is 20 nm larger than expected. This difference was likely introduced during the exposure of the mask or wafer. Measurements from all three sets of parameters indicate that the third recipe is optimal for etching photonic crystals in c-Si.

Table 4.1 Photonic crystal lattice measurements after c-Si etching

| Recipe | Etch Depth (nm) | Pitch (nm) | Diameter (nm) | Spacing (nm) | $R/a$ |
|---|---|---|---|---|---|
| Ideal | 250 | 740 | 445 | 300 | 0.300 |
| 1 | 200 | 760 | 565 | 190 | 0.372 |
| 1 | 220 | 760 | 615 | 140 | 0.405 |
| 2 | 250 | 760 | 565 | 195 | 0.372 |
| 3 | 250 | 760 | 555 | 200 | 0.365 |

### 4.1.2 Ag/ZnO:Al Processing

After etching and cleaning, 50 nm of Ag was thermally evaporated and 100 nm of ZnO:Al was sputtered on the substrates. As shown in Figure 4.2(a), the Ag evaporation appeared to be uniform across the surface of the c-Si wafer. Slight texturing was introduced where small particles were covered with Ag, but the size of these particles were well below the minimum feature size of the photonic crystal. Additional roughness was observed at the bottom of the etched cavities. This was thought to be caused by Ag either evaporating on small particles or settling in the cavity instead of on the side-walls during the evaporation. Figure 4.2(b) shows the same substrate after ZnO:Al was sputtered on the surface. The ZnO:Al film uniformly coated the etched features and did not appear to be textured. Since sputtering is typically an omnidirectional deposition process, sufficient side-wall coverage and uniformity was expected.

#### 4.1.2.1 Side-wall coverage

The $R/a$ after Ag evaporation was found to decrease from 0.37 to 0.36, which indicated that approximately 10 nm to 15 nm was deposited on the side-walls. An additional drop was measured after sputtering ZnO:Al, which resulted in a final $R/a$ of 0.32 before the a-Si:H device was deposited. Therefore, an estimated 30 nm of ZnO:Al was deposited on the side-walls. Due to the limited resolving capabilities and resolution of the SEM, these values have a non-negligible amount of error. Cross-sectional images from a higher

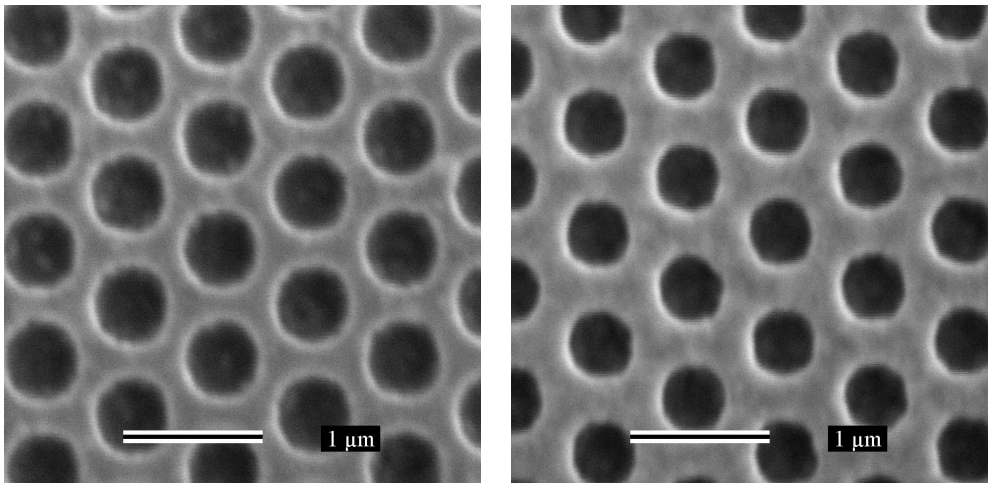


(a) (b)

Figure 4.2 SEMs of photonic crystal back-reflector after 50 nm thick Ag was evaporated (a) and 100 nm thick ZnO:Al was sputtered (b). (25,000x magnification and 1$\mu$m scale)

resolution SEM would provide a more accurate measure of side-wall coverage.

### 4.1.3 Reflective Properties

Diffuse and total reflection was also measured after Ag was evaporated to characterize the reflective properties of the metallic photonic crystal. Absorption can also be measured from total reflectance if the assumption is made that light is not transmitted through the back-reflector.

As shown in Figure 4.3(a), total reflection at longer wavelengths was similar to flat Ag. As the wavelength of incident light approached the pitch of the photonic crystal, significant absorption resulted from standing waves in the photonic crystal cavities [5, 6]. Diffuse reflectance appeared to increase precipitously until it reached a maximum of 81% at 545 nm. Absorption below the lattice pitch and intense diffuse reflectance were designed properties of this photonic crystal back-reflector.

There were several discrepancies between the measured and simulated photonic crystal reflective properties. The measured peak in absorption was lower than the predicted

amount, as shown in Figure 4.3(b). This was probably due to slight variations within the photonic crystal lattice, which would broaden and potentially lower the absorption distribution. A second, smaller peak in diffuse reflection was also observed and can be attributed to variations as well. Total reflection at longer wavelengths ($\lambda > 750$ nm) was also larger than expected. This increase in total reflection is not necessarily a loss, since a-Si:H weakly absorbs at these wavelengths and the surface will resemble a flat silver back-reflector.

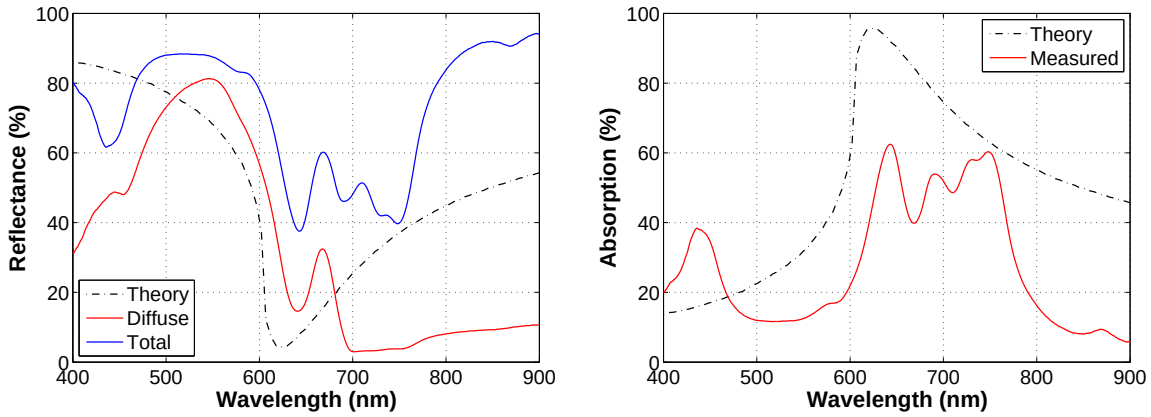


(a) (b)

Figure 4.3 Diffuse and total reflectance of the photonic crystal back-reflector after Ag evaporation is shown in (a). Absorption of the photonic crystal is shown in (b). Simulated data is shown for a triangular lattice photonic crystal with $a = 700$ nm.

## 4.2 a-Si:H Devices on Back-reflector Substrates

Several a-Si:H *n-i-p* solar cell devices were deposited on photonic crystal substrates that were prepared with the first and second set of plasma etching parameters, which had etch depths of 200 nm, 220 nm, and 250 nm[1]. Measurements were performed to

[1]MRC Device ID: 200 nm = 2/12112, 220 nm = 2/12183, 250 nm = 2/12257

determine absorption enhancement and I-V characteristics. SEM images were also taken to characterize the a-Si:H device deposition and side-profile.

### 4.2.1 SEM Analysis

After the a-Si:H devices were fabricated, SEM images were taken to investigate the surface and side-profile. As shown in Figure 4.4(a), the deposited a-Si:H and ITO conformally coated the photonic crystal back-reflector. The lattice was still evident on the surface of the device, with pinhole features present where the c-Si was previously etched. A textured surface was expected, as the etch depth of the cavities was approximately half of the total a-Si:H device thickness. The side-profile for a similar device is shown in Figure 4.4(b). In this image, the etched cavities are clearly present and filled with a-Si:H. The conformal a-Si:H deposition is also depicted with the profile of the pinhole features.

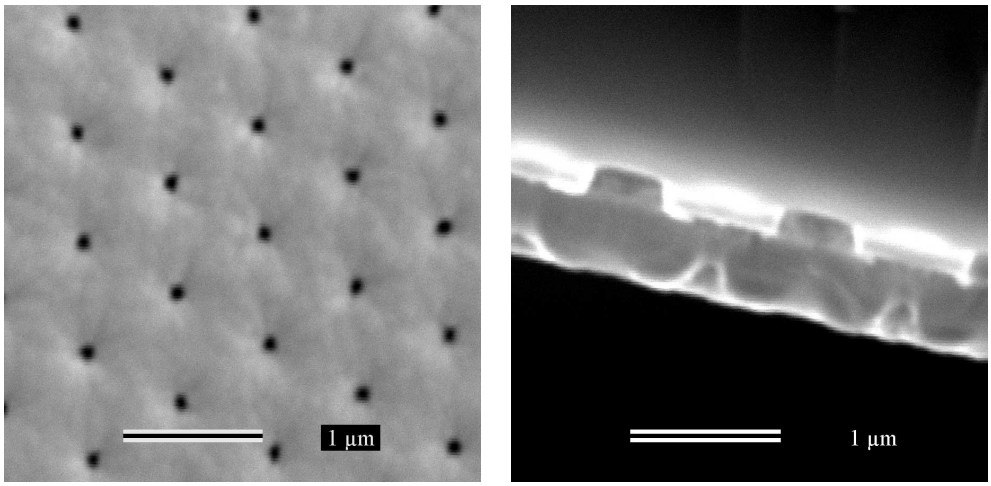


(a) (b)

Figure 4.4 SEMs of photonic crystal back-reflector after a-Si:H device deposition and ITO sputtering. The device surface is shown in (a) and the side-profile is shown in (b). (1 $\mu$m scale)

### 4.2.2 EQE and I-V Measurements

EQE and I-V measurements were performed to characterize the a-Si:H devices. Each substrate had at least two devices on the photonic crystal back-reflector and one reference device on flat Ag/ZnO:Al. With the flat reference on the photonic crystal substrate, enhanced light trapping and absorption was determined by comparing identical a-Si:H devices.

#### 4.2.2.1 200 nm Etch Depth

An a-Si:H solar cell was deposited on a back-reflector substrate prepared with the first set of etching parameters. This substrate had an etch depth of 200 nm and the i-layer thickness of the a-Si:H device was approximately 220 nm. After the device was deposited and ITO contacts were sputtered, I-V and EQE were measured for both photonic crystal back-reflector devices and the reference device.

I-V measurements indicated an increase in short circuit current, from 10.86 mA/cm$^2$ for the reference device to 13.88 mA/cm$^2$ and 12.92 mA/cm$^2$ for the back-reflector devices. These contacts over the photonic crystal were slightly diffused, which resulted in larger current density measurements with the I-V apparatus. Shadowing from the top contact probe was also not accounted for, which may explain variation in the back-reflector measurements. Open circuit voltage and fill factor decreased when a back-reflector was used. The fill factor of the reference device was 58% while the photonic crystal devices had fill factors of 52%. Open circuit voltage decreased from 0.84 V for the reference to 0.77 V for the back-reflector devices. This decrease in $V_{oc}$ is typically observed with textured back-reflectors in thin-film solar cells and may be attributed to a greater reverse saturation current in the reference device. The shunt resistance also decreased, which indicated that additional low resistance paths were introduced in the a-Si:H i-layer on the back-reflector substrate.

As shown in Figure 4.5, the photonic crystal back-reflector device significantly improved EQE for wavelengths longer than 620 nm. The enhancement in EQE extended to wavelengths near the a-Si:H band edge. The similarity in EQE at lower wavelengths is expected since lower wavelength photons are typically absorbed before reaching the back-reflector. A slight decrease in EQE was found near 600 nm. This may be attributable to absorptive losses in the back-reflector. The EQE short circuit current was found to be 13.22 mA/cm$^2$ and 13.17 mA/cm$^2$ for the photonic crystal back-reflector devices and 12.27 mA/cm$^2$ for the reference device. This corresponded to a 7.7% and 7.3% increase in EQE $J_{sc}$, which is more accurate than the improvement shown with I-V measurements.

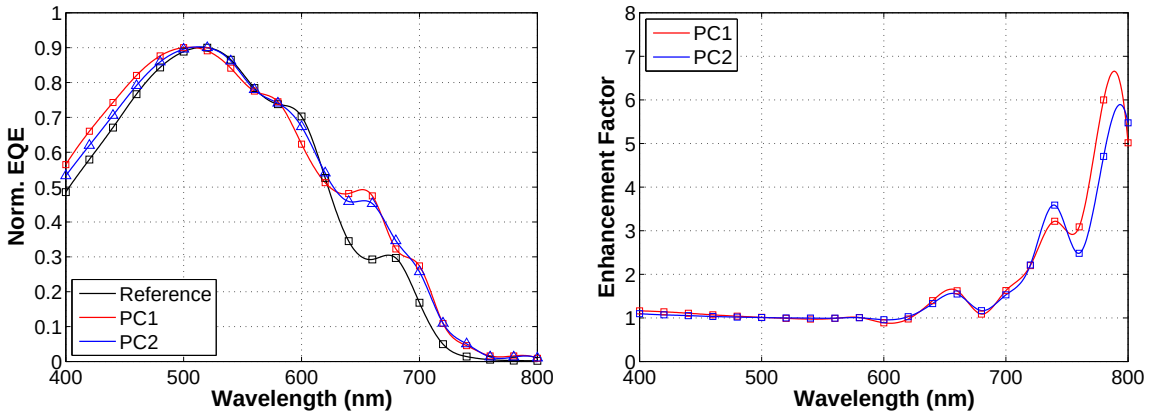


(a) (b)

Figure 4.5 Normalized EQE for a-Si:H photonic crystal back-reflector devices with 200 nm etch depth and flat reference (a). The enhancement factor for both back-reflector devices is shown in (b).

Absorption enhancement was determined by taking the following ratio at each measured wavelength:

$$\text{Enhancement Factor}(\lambda) = \frac{EQE(\lambda)_{PC}}{EQE(\lambda)_{Ref}} \tag{4.1}$$

where $EQE(\lambda)_{PC}$ is EQE for devices on the photonic crystal back-reflector and $EQE(\lambda)_{Ref}$ is EQE for the reference device. This enhancement factor is plotted in Figure 4.5(b)

and has two distinct resonances for both substrates. A factor of 4 improvement in EQE was found at 740 nm. The second resonance was at 780 nm and increased the EQE by a factor of 6.

#### 4.2.2.2 250 nm Etch Depth

An a-Si:H device was also deposited on a photonic crystal back-reflector substrate that was etched with the second set of parameters. The c-Si etch time was increased to achieve an etch depth of 220 nm and the i-layer thickness was 290 nm.

An improvement in $J_{sc}$ was found with I-V measurements, from 12.98 mA/cm$^2$ for the reference device to 13.14 mA/cm$^2$ and 13.46 mA/cm$^2$ for the back-reflector devices. Unlike the previously discussed device, these contacts were not diffused. A similar decrease in fill factor was observed with these devices. The fill factor of the reference device was 60% while both photonic crystal devices had fill factors of 50%. Open circuit voltage also decreased from 0.84 V to 0.79 V for the reference and back-reflector devices, respectively.

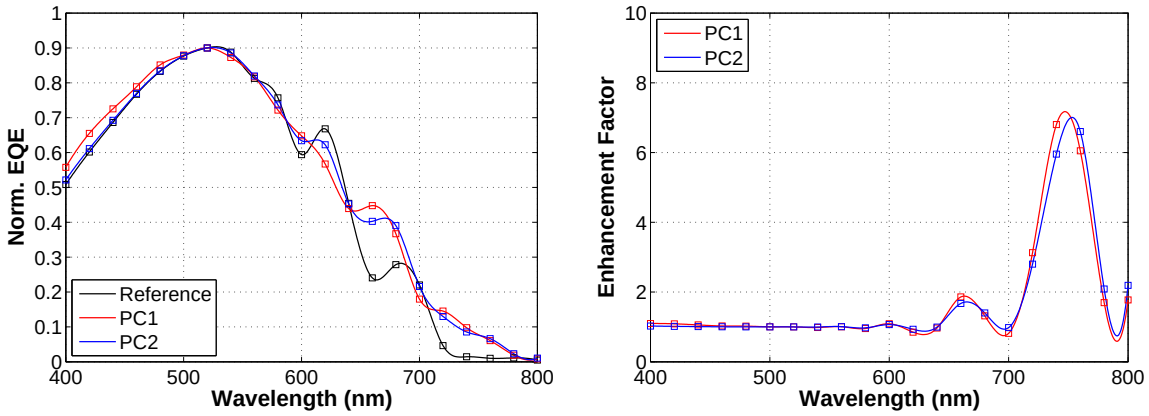


(a) (b)

Figure 4.6 Normalized EQE for a-Si:H photonic crystal back-reflector devices with 250 nm etch depth and flat reference (a). The enhancement factor for both back-reflector devices is shown in (b).

The normalized EQE for this device is shown in Figure 4.6(a). Similar to devices deposited on the substrate with an etch depth of 200 nm, the EQE was similar for wavelengths shorter than 600 nm and diverged at longer wavelengths. The photonic crystal back-reflector devices did not demonstrate a decrease in EQE near 600 nm and 660 nm, which is introduced by destructive interference of standing waves in the a-Si:H layer. A shoulder in the EQE at 640 nm resulted in significant enhancement in EQE at red and near-infrared wavelengths. These devices had two distinct enhancement resonances and is shown in Figure 4.6(b). A minor peak at 660 nm had an enhancement of 2 over the reference device. The second peak was located near 740 nm and had a factor of 7 improvement in EQE. The EQE short circuit current was found to be 13.30 mA/cm$^2$ for the photonic crystal back-reflector devices and 12.59 mA/cm$^2$ for the reference device. This corresponded to a 5.6% increase in EQE $J_{sc}$.

#### 4.2.2.3 220 nm Etch Depth with a Flat Ag Reference

An additional a-Si:H device was deposited on a photonic crystal back-reflector substrate that had an etch depth of 220 nm. The substrate was fabricated using the first set of etching parameters and the i-layer thickness of the device was 200 nm. The flat reference did not produce measurable devices, so an identical device was deposited on a stainless steel substrate that was coated with 50 nm of Ag.

As expected, I-V measurements indicated that there was an improvement in $J_{sc}$ between the photonic crystal and flat Ag back-reflectors. This increase in current density was greater than devices with a flat Ag/ZnO reference, mainly due to heavily diffused contacts on the photonic crystal back-reflector devices. The reference device on flat Ag had a fill factor of 67% and a shunt resistance of 15 KΩ. The photonic crystal back-reflector device had a fill factor of 50%, which was typical for devices in this research. The shunt resistance was 2.3 KΩ, which was significantly lower than the reference and approximately half the resistance of the previously discussed back-reflector devices.

Open circuit voltage also decreased from 0.85 V for the reference device to 0.80 V for the photonic crystal back-reflector device.

The EQE in Figure 4.7(a) shows significant improvement in absorption for long wavelength photons. Two distinct shoulders are present at 600 nm and 680 nm, where the photonic crystal back-reflector device offered enhanced absorption where the flat Ag reference device decreased in EQE. As shown in Figure 4.7(b), peak enhancement occurred at the second shoulder with a factor of 8 improvement at 720 nm. A second sub-peak was present at 760 and had a factor of 6 improvement in EQE. Enhancement decreased near 800 nm, but absorption is very weak in a-Si:H for these wavelengths. The EQE short circuit current was found to be 13.38 mA/cm$^2$ for the photonic crystal back-reflector device and 12.17 mA/cm$^2$ for the reference device. This corresponded to a 10% increase in EQE $J_{sc}$.

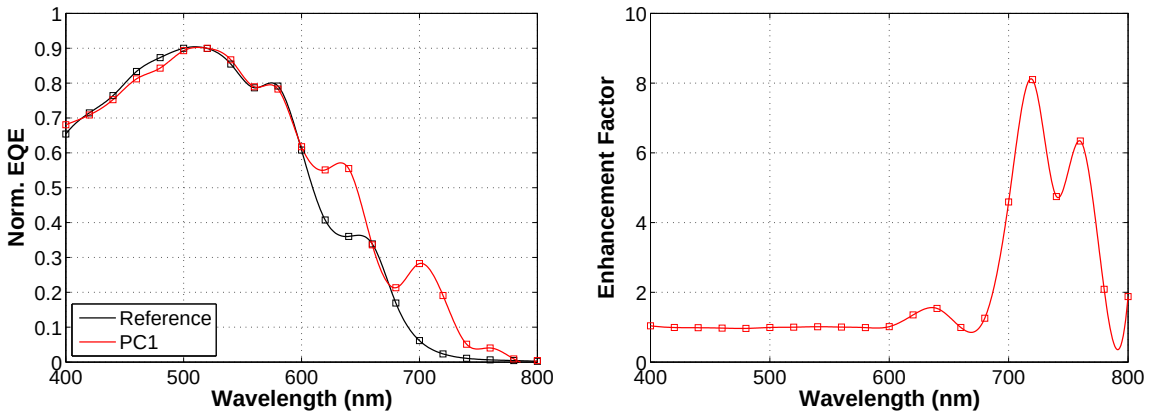


(a) (b)

Figure 4.7 Normalized EQE for an a-Si:H photonic crystal back-reflector device with 220 nm etch depth and a flat Ag reference on stainless steel (a). The enhancement factor for both back-reflector devices is shown in (b).

### 4.2.3 Device Comparison

A summary of the a-Si:H device data is shown in Table 4.2. From this table, it is clear that a-Si:H devices deposited on photonic crystal back-reflectors has a significantly higher EQE $J_{sc}$ compared to their respective flat reference devices. This increase in $J_{sc}$ was attributed to absorption enhancement of red and near-infrared photons. The largest improvement in $J_{sc}$ was found with devices on the photonic crystal back-reflector that was etched 220 nm, but this substrate did not have a measurable Ag/ZnO:Al reference. The a-Si:H devices that had a reference device on the photonic crystal substrate were found to have similar improvements in $J_{sc}$. Peak enhancement was also comparable for these devices, with the device deposited on the 250 nm etch depth substrate performing slightly better. All photonic crystal back-reflector devices suffered from a decrease in $V_{oc}$ and $f.f.$, with respect to their reference devices.

Table 4.2 Summary of device I-V and EQE results.

| | Etch Depth (nm) | i-layer Thickness (nm) | $V_{oc}$ (V) | EQE $J_{sc}$ (mA/cm$^2$) | $f.f.$ | Peak Enhancement |
|---|---|---|---|---|---|---|
| PC1 | 200 | 220 | 0.77 | 13.22 | 51.4 | 6 |
| PC2 | 200 | 220 | 0.77 | 13.17 | 52.0 | 5.6 |
| Ref. | - | 220 | 0.84 | 12.27 | 58.3 | - |
| PC1 | 250 | 290 | 0.78 | 13.30 | 49.4 | 6.8 |
| PC2 | 250 | 290 | 0.79 | 13.28 | 49.6 | 6.6 |
| Ref. | - | 290 | 0.84 | 12.59 | 60.6 | - |
| PC1 | 220 | 200 | 0.80 | 13.38 | 50.0 | 8 |
| Ref. | - | 200 | 0.85 | 12.17 | 67.0 | - |

# CHAPTER 5. CONCLUSIONS AND FUTURE WORK

Photonic crystal back-reflectors were fabricated and implemented in a-Si:H solar cells as a means to enhance absorption at long wavelengths. Silicon wafers were patterned with photolithography and etched with a $CF_4/O_2$ plasma to form the triangular lattice photonic crystals. Silver was then evaporated on the etched substrates to form a highly reflective back contact. Aluminum doped zinc oxide was also sputtered on the silver reflector to prevent agglomeration during subsequent high temperature processing. The photonic crystal pitch and filling ratio were measured with scanning electron microscopy and found to be 760 nm and 0.31, respectively. The processed back reflector structures had high-quality long-range periodicity. Amorphous silicon devices were deposited on the back-reflectors using plasma enhanced chemical vapor deposition. Indium tin oxide was then sputtered on the devices as a top contact and antireflection coating.

Diffuse and total reflection measurements indicated that the photonic crystal substrates had over 60% diffuse reflection between 500 nm and 600 nm, with peak of 81% near 550 nm. A decrease in total reflection between 600 nm and 800 nm was also measured and can be attributed to absorption within the photonic crystal due to standing waves in the cavities. Several a-Si:H devices were deposited on the photonic crystal back-reflector and characterized with I-V and external quantum efficiency measurements. I-V and EQE measurements showed that the photonic crystal back-reflector increased short circuit current by 10% with respect to a flat Ag reference. A 7.7% increase in short circuit current was measured for flat Ag/ZnO:Al reference devices on the photonic crystal substrate. Significant enhancement in long wavelength ($\lambda > 650$ nm) absorption

was also observed, with up to a factor of 7 improvement at certain wavelengths when compared to an identical device with a flat Ag/ZnO:Al back-reflector. The photonic crystal enhanced long wavelength absorption by a factor of 8 for an Ag coated stainless steel reference device. Additionally, absorption enhancement was observed between 650 nm and 800 nm for every fabricated substrate. A decrease in open circuit voltage and fill factor occurred with devices deposited on the photonic crystal back-reflectors, and should be minimized with additional research.

**Future Work** In this research, a wide range of substrate fabrication parameters was investigated to further enhance absorption. Several aspects of the photonic crystal back-reflectors were identified as potential losses, including the depth of the etched cavities, Ag thickness and side-wall coverage, and thickness of the n-type a-Si:H layer. While some of these issues were explored, a thorough analysis was not possible with the limited number of available substrates. Suggestions for future research are discussed in the order of their perceived priority.

In a study on nc-Si:H growth and defects by Python, voids and cracks formed during nc-Si:H depositions on periodic back-reflector surfaces [25]. A relationship between cracks and solar cell performance was found, as fill factor and open circuit voltage decreased when the crack density increased. Although there is a difference between a-Si:H and nc-Si:H solar cell thickness, the photonic crystal cavity etch depth is nearly half of the total solar cell thickness. Issues with a-Si:H growth on the rough back-reflector surface may be responsible for the decrease in fill factor and open circuit voltage. Determining the effect of etch depth on electrical properties of the a-Si:H solar cell is highly suggested for future work. Transmission electron microscopy would also be beneficial in characterizing a-Si:H growth on photonic crystal back-reflectors.

Although evaporated Ag films were typically smooth and had high reflectance, thickness on the cavity side-walls was a concern. As discussed in Section 4.1.2.1, the esti-

mated side-wall Ag coverage was 10 nm to 15 nm. An Ag film of this thickness is fairly transmissive, which may result in significant optical losses at lower wavelengths where a back-reflector is beneficial. A 100 nm thick Ag layer was also evaporated on several photonic crystal substrates and eventually agglomerated while ZnO:Al was sputtered. Thin ZnO:Al appeared to reduce intial agglomeration, but the Ag agglomerated during the device deposition. Future research might expand on these findings and determine optimal Ag and ZnO:Al thicknesses that have minimal transmission and are not prone to agglomeration. Sputtering would be ideal for depositing a uniform film on photonic crystals and might be investigated as well. Ag agglomeration may also be reduced by RCA cleaning the substrates before evaporation.back-reflector

The 250 nm thick n-type a-SiC:H layer was also thought to have filled the photonic crystal cavities. Simulation results indicated that standing waves contribute to absorption enhancement between 650 nm and 750 nm with an absorber layer in the cavities. Since n-type a-SiC:H has an even larger bandgap than a-Si:H and suffers from significant hole recombination, enhancement due to standing waves will be minimal. Future work might attempt to reduce the n-layer thickness, which would effectively increase the i-layer presence in the cavities.

# APPENDIX

# ALTERNATIVE CLEANING METHODS

As previously mentioned, small particles were found on the c-Si surface immediately after etching and plasma cleaning. The number of particles in a given area of the substrate not only varied between RIE runs, but appeared to increase throughout the span of this research. The $O_2$ plasma cleaning plasma parameters were modified several times with little to no success in reducing the number of particles on the surface. After it was determined that the particles were not introduced during plasma cleaning, the possibility of particles introduced during etching was tested. A substrate was ultrasonicated in acetone to remove the remaining photoresist immediately after it was etched. The substrate was then ultrasonicated in methanol and dried with nitrogen to clean the surface of debris. A standard 5 minute $O_2$ plasma was used to remove the BARC layer. As shown in Figure A.1, this method eliminated the particle issue. Large streaks were seen across the substrate, which may indicate that a cleaner processing area is needed if this method is used.

An RCA clean was also found to help Ag evaporate uniformly across the substrate. Immediately after the substrate was etched and cleaned with an $O_2$ plasma, the following cleaning process was used:

- 1:1:5 solution of $NH_4OH$ + $H_2O_2$ + $H_2O$ at 85°C for 15 minutes
- $H_2O$ rinse for 3 minutes

- 50:1 solution of HF + $H_2O$ for 15 seconds
- $H_2O$ rinse for 1 minute
- 1:1:6 solution of HCl + $H_2O_2$ + $H_2O$ at 85°C for 15 minutes
- $H_2O$ rinse for 3 minutes

While extensive testing was not performed with this cleaning method, reflection data indicated that the Ag film after RCA cleaning was superior to evaporated Ag on substrates that were ultrasonicated in methanol. SEMs should be taken to further characterize this additional process.

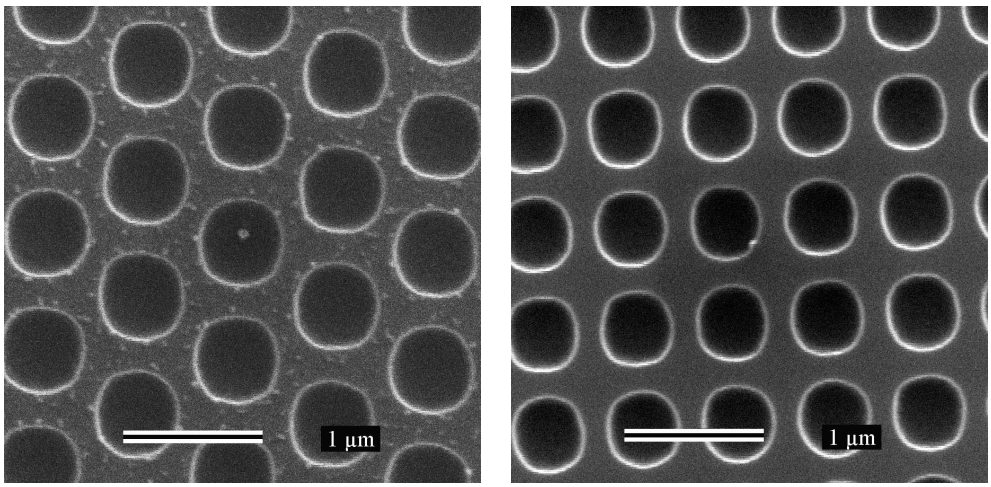


(a) (b)

Figure A.1 SEMs of c-Si photonic crystals after $O_2$ plasma cleaning (a) and acetone/methanol photoresist strip and $O_2$ cleaning (b). (25,000x magnification and 1$\mu$m scale)

# BIBLIOGRAPHY

[1] "International energy outlook 2009 - world energy demand and economic outlook," http://www.eia.doe.gov/oiaf/ieo/world.html, Energy Information Administration.

[2] B. Rech and H. Wagner, "Potential of amorphous silicon for solar cells," *Applied Physics A: Materials Science & Processing*, vol. 69, no. 2, pp. 155–167, 1999.

[3] D. Zhou and R. Biswas, "Photonic crystal enhanced light-trapping in thin film solar cells," *Journal of Applied Physics*, vol. 103, p. 093102, 2008.

[4] R. Biswas, C. Ding, I. Puscasu, M. Pralle, M. McNeal, J. Daly, A. Greenwald, and E. Johnson, "Theory of subwavelength hole arrays coupled with photonic crystals for extraordinary thermal emission," *Physical Review B*, vol. 74, no. 4, p. 45107, 2006.

[5] A. Ferlauto, G. Ferreira, J. Pearce, C. Wronski, R. Collins, X. Deng, and G. Ganguly, "Analytical model for the optical functions of amorphous semiconductors from the near-infrared to ultraviolet: Applications in thin film photovoltaics," *Journal of Applied Physics*, vol. 92, p. 2424, 2002.

[6] P. Bermel, C. Luo, L. Zeng, L. Kimerling, and J. Joannopoulos, "Improving thin-film crystalline silicon solar cell efficiencies with photonic crystals," *Optics Express*, vol. 15, no. 25, pp. 16 986–17 000, 2007.

[7] L. Zeng, Y. Yi, C. Hong, J. Liu, N. Feng, X. Duan, L. Kimerling, and B. Alamariu, "Efficiency enhancement in Si solar cells by textured photonic crystal back reflector," *Applied Physics Letters*, vol. 89, p. 111111, 2006.

[8] L. Zeng, P. Bermel, Y. Yi, B. Alamariu, K. Broderick, J. Liu, C. Hong, X. Duan, J. Joannopoulos, and L. Kimerling, "Demonstration of enhanced absorption in thin film Si solar cells with textured photonic crystal back reflector," *Applied Physics Letters*, vol. 93, p. 221105, 2008.

[9] J. Krc, M. Zeman, S. Luxembourg, *et al.*, "Modulated photonic-crystal structures as broadband back reflectors in thin-film solar cells," *Applied Physics Letters*, vol. 94, p. 153501, 2009.

[10] M. Berginski, J. Hupkes, M. Schulte, G. Schope, H. Stiebig, B. Rech, and M. Wuttig, "The effect of front zno:al surface texture and optical transparency on efficient light trapping in silicon thin-film solar cells," *Journal of Applied Physics*, vol. 101, no. 7, p. 074903, 2007.

[11] B. Yan, J. Owens, C. Jiang, J. Yang, and S. Guha, "Improved Back Reflector for High Efficiency Hydrogenated Amorphous and Nanocrystalline Silicon Based Solar Cells," *Amorphous and Nanocrystalline Silicon Science and Technology– 2005*, vol. 862, pp. 603–608, 2005.

[12] F. Haug, V. Terrazzoni-Daudrix, T. Söderström, X. Niquille, J. Bailat, and C. Ballif, "Flexible microcrystalline silicon solar cells on periodically textured plastic substrates," *Proceedings of the 21st European PVSEC*, vol. 1651, 2006.

[13] E. Yablonovitch and G. Cody, "Intensity enhancement in textured optical sheets for solar cells," *IEEE Transactions on Electron Devices*, vol. 29, no. 2, pp. 300–305, 1982.

[14] J. Nelson, *The physics of solar cells*. Imperial College Press, 2003.

[15] J. Springer, A. Poruba, L. M
"ullerova, M. Vanecek, O. Kluth, and B. Rech, "Absorption loss at nanorough silver back reflector of thin-film silicon solar cells," *Journal of Applied Physics*, vol. 95, p. 1427, 2004.

[16] H. Park, K. Kwon, S. Lee, B. Koak, S. Nahm, H. Lee, K. Cho, O. Kwon, and Y. Kang, "A study on modified silicon surface after $CHF_3/C_2F_6$ reactive ion etching," *ETRI J*, vol. 16, no. 1, p. 45, 1994.

[17] R. Knizikevičius, "Real dimensional simulation of silicon etching in $CF_4$+$O_2$ plasma," *Applied Surface Science*, vol. 201, no. 1-4, pp. 96–108, 2002.

[18] J. Plummer, M. Deal, and P. Griffin, "Silicon VLSI technology," 2008.

[19] M. Bass, E. Van Stryland, D. Williams, and W. Wolfe, *Handbook of optics. Vol. 2, Devices, measurements, and properties*. McGraw-Hill New York, USA, 1995.

[20] D. Adams, T. Alford, and J. Mayer, *Silver Metallization: Stability and Reliability*. Springer, 2008.

[21] K. Sieradzki, K. Bailey, and T. Alford, "Agglomeration and percolation conductivity," *Applied Physics Letters*, vol. 79, p. 3401, 2001.

[22] R. Boesch, "$SiO_2$ nanosphere textured back reflectors for enhanced light trapping in amorphous and nanocrystalline silicon solar cells," Master's thesis, Iowa State University, 2009.

[23] C. Honsberg and S. Bowden, "Illumination Sources," http://pvcdrom.pveducation.org/CHARACT/illum.htm.

[24] B. Streetman, *Solid state electronic devices*, 1995.

[25] M. Python, "Microcrystalline silicon solar cells: Growth and defects," Ph.D. dissertation, Université de Neuchâtel, 2009.